SEISMOLOGY AND ACOUSTIC-GRAVITY WAVES

David G. Harkrider

California Institute of Technology

Prepared for:

Air Force Office of Scientific Research
Advanced Research Projects Agency

31 December 1973

California Institute of Technology
Division of Geological and Planetary Sciences
Seismological Laboratory
Pasadena, California 91109

SEMI-ANNUAL TECHNICAL REPORT

1 July 1972 - 31 December 1973

ARPA Order No:	846
Program Code:	OFIO
Name of Contractor:	California Institute of Technology
Effective Date of Contract:	1 July 1970
Contract Expiration Date:	30 June 1973
Amount of Contract:	$52,749
Contract Number:	F44620-70-C-0120
Principal Investigator and Phone Number:	David G. Harkrider (213) 795-8806
Program Manager and Phone Number:	William J. Best (202) 694-5456
Short Title of Work:	Seismology and Acoustic-Gravity Waves

Approved for public release; distribution unlimited.

Sponsored by
Advanced Research Projects Agency
ARPA Order No. 346

UNCLASSIFIED

SECURITY CLASSIFICATION OF THIS PAGE (When Data Entered)

-1-

AD-779939

REPORT DOCUMENTATION PAGE

READ INSTRUCTIONS BEFORE COMPLETING FORM

1. REPORT NUMBER	2. GOVT ACCESSION NO. / 3. RECIPIENT'S CATALOG NUMBER
4. TITLE (and Subtitle) SEISMOLOGY AND ACOUSTIC-GRAVITY WAVES	5. TYPE OF REPORT & PERIOD COVERED Semi-Annual Technical Report 1 July 1972-31 December 1973 6. PERFORMING ORG. REPORT NUMBER
7. AUTHOR(s) David G. Harkrider	8. CONTRACT OR GRANT NUMBER(s) F44620-70-C-0120
9. PERFORMING ORGANIZATION NAME AND ADDRESS California Institute of Technology Seismological Laboratory P.O. Bin 2-Arroyo Annex, Pasadena, Calif. 91109	10. PROGRAM ELEMENT, PROJECT, TASK AREA & WORK UNIT NUMBERS ARPA Order 846 Program Code OF10 Program Element Code 62701D
11. CONTROLLING OFFICE NAME AND ADDRESS AFOSR 1400 Wilson Blvd. (NPG) Arlington, Virginia 22209	12. REPORT DATE 13. NUMBER OF PAGES 109
14. MONITORING AGENCY NAME & ADDRESS(if different from Controlling Office)	15. SECURITY CLASS. (of this report) Unclassified 15a. DECLASSIFICATION/DOWNGRADING SCHEDULE

16. DISTRIBUTION STATEMENT (of this Report)

Approved for public release; distribution unlimited.

17. DISTRIBUTION STATEMENT (of the abstract entered in Block 20, if different from Report)

18. SUPPLEMENTARY NOTES

19. KEY WORDS (Continue on reverse side if necessary and identify by block number)

Underground explosions
Stochastic inverse applied to surface displacements
Excitation of Rayleigh waves
Excitation of acoustic gravity waves
Alaskan earthquake mechanism, finite element approach

20. ABSTRACT (Continue on reverse side if necessary and identify by block number)

Previous reports under the project have shown that in order to make realistic estimates of acoustic gravity waves and seismic surface waves generated by underground events, such as explosions and earthquakes, the change in surface displacement field or the source parameters of the event must be obtained. Surface displacement data for actual events is usually limited and of dubious quality.

DD FORM 1 JAN 73 1473 EDITION OF 1 NOV 65 IS OBSOLETE

UNCLASSIFIED

SECURITY CLASSIFICATION OF THIS PAGE (When Data Entered)

CONTENTS

I. Summary

Previous reports under the project have shown that in order to make realistic estimates of acoustic gravity waves and seismic surface waves generated by underground events, such as explosions and earthquakes, the change in surface displacement field or the source parameters of the event must be obtained. Surface displacement data for actual events is usually limited and of dubious quality.

Section II deals with the development of a systematic approach of determining the dislocation or relative displacement on the fault surface from a limited set of observed surface displacement data with their estimated errors. The technique gives not only a best fit dislocation model but allows one to determine the reliability of the model and the resolving power of the data set. The resulting dislocation model can then be used to extrapolate the surface displacements outside of the data set.

Section III deals with the applications of the inversion technique described in the previous section to the change in surface displacement data caused by deformation resulting from the 1964 Alaska earthquake. For this earthquake, a two-dimensional finite element numerical model is used to calculate surface displacements from a dislocation imposed on a fault surface located in a heterogeneous medium. The inversion technique is used to calculate a dislocation model which fits the observed data to a high degree of accuracy. An error analysis is carried out for the plain-strain approximation, and the resolvability of the features of the calculated dislocation is examined. The results indicate that the observed deformation occurred

as the result of massive underthrusting of the Alaska continental block by the downgoing Pacific plate.

Sections II and III are chapters II and III of Ralph Wilson Alewine, III's Thesis (1974) titled "Application of Linear Inversion Theory Toward the Estimation of Seismic Source Parameters". References and details cited in these sections can be found in the Thesis. This thesis has been submitted and successfully defended as partial fulfillment of the requirements for the Degree of Doctor of Philosophy at the California Institute of Technology, Pasadena, California.

Chapter 2

Development of the Stochastic Inverse as Applied to Static Dislocation Problems

2.1 Introduction.

The first requisite in the application of any theory toward the estimation of seismic source parameters is the ability to solve the forward problem for the observed data type for an appropriate seismic source. This means simply that given a certain method of physically describing a source (analytically, numerically, or by analogue) we are able to estimate changes in data for a given value, or change in value, of particular parameters which describe the source. Mathematically this is mapping changes in the source model space into changes in the data space. What will be discussed first in this chapter is just this process, and later we will look at the inverse of this process. By the inverse of this process, we mean that given some observations, what estimates can be made about the different source parameters which describe our source?

The inversion scheme for static data that we propose in this chapter has the provision for the inclusion of the estimated variance of the data that is to be inverted. The inclusion of this data variance gives rise to the

fact that we cannot now estimate the seismic source parameters exactly, since small perturbations in the model source parameters might cause changes in the calculated data values which lie inside the estimated data error limits. This concept gives rise to our wondering what ability that we have to actually resolve any detail of the various parameters of our fault model. This resolution question will be examined in some detail in this chapter.

We will first consider the problem of estimating source parameters for static data. The procedure developed for this case can then be extended to that of estimating dynamical source parameters. This extension is done in a later chapter. A brief review of the development of static field solutions due to various earthquake sources is in order.

2.2 Development of the Forward Static Problem.

Numerous attempts have been made in the past several years to interpret the observed permanent changes in the displacement and strain fields due to the occurrence of an earthquake. Various approaches to the solution of this problem have been proposed, each based on a slightly different interpretation of the earthquake source process as a whole. In each of these approaches, there exists in the interior of the elastic medium some discontinuity

surface which we can associate with a "fault". The different initial or boundary conditions that can be applied to this discontinuity surface give rise to the various approaches. These approaches can be broken into four main groups: stress pulse theory, stress relaxation theory, dislocation theory, and numerical analogues. With the exception of the dislocation theory, which wil be treated in more detail, a short description of the approach of each of these theories will be presented. The dislocation theory is reviewed in more detail because it involves a parameter that is readily observable when the discontinuity surface breaks the free surface -- a physical offset. In addition, it is somewhat more straightforwardly pleasing to model static dislocations on the surface caused by static dislocations imposed within the medium rather than the more obscure parameters -- stress and strain. However, it will be seen that the other theoretical approaches can be equivalenced to some dislocation representation in the static limit.

Dislocation Theory. As a mathematical model of a "fault", the concept and formulation of a physical dislocation has been extensively used. The dislocation surface in an elastic medium is viewed as a surface over which there is a discontinuity in displacement. One of the first efforts

to explain the elastic displacements resulting from a dislocation was that done by Vvendenskaya (1956, 1958). Probably the most lucid explanation of the dislocation theory for calculating static changes that accompany faulting was given in a set of papers by Steketee (1958a, 1958b). In these papers, Steketee recognized that the relations for the displacement field in an infinite elastic medium strained by a dislocation over some surface as given earlier by Volterra (1907) would be appropriate in describing the deformation that accompanies faulting. Steketee derived, through the use of Galerkin vectors, the expressions for static displacements in an infinite elastic solid. These relations were given in compact form as integrals over the dislocation surface.

In his papers, Steketee poses the following problem. A dislocation surface, Σ , is created with an elastic solid which is bounded by some surface S . The media is then strained by the introduction of a certain distribution of "nuclei of strain" (Love, 1944) along the dislocation surface. The nuclei were shown to exist in six basic forms corresponding broadly to a combination of a center of dilatation and a double force without moment, and secondly, two coplanar, mutually perpendicular double forces with moments. For pure shear dislocations, only

the latter type nuclei are applicable, whereas, for pure tensile dislocations, the former are applicable. The displacements at a point Q, $u_k(Q)$, within the elastic solid can be written as

$$u_k(Q) = \frac{1}{8\pi\mu}\iint_{\Sigma} \Delta u_i(P)\omega_{ij}^k(P,Q)\nu_j d\Sigma - \frac{1}{8\pi\mu}\iint_{S} u_i\omega_{ij}^k(P,Q)\nu_j ds \quad . \tag{2.1}$$

In this equation ν_j are the direction cosines of the normal to the dislocation surface elements, μ is the rigidity, and $\Delta u_i(P)$ is the dislocation function on the surface Σ. It is seen that for an arbitrary dislocation, a set of six of these functions is necessary. (i=1,2,3 j=1,2,3 with ij=ji.) The kernels of the integrals, $\omega_{ij}^k(P,Q)$, are the displacements at the observation point due to a single nucleus of strain. A summation over all nuclei is implied. As the surface S is enlarged to infinity, the displacements, u_i, on S approach zero and the second integral vanishes.

The formalism for this problem was extended to include a dislocation in a semi-infinite elastic medium by a

superposition of solutions, which together satisfy the required boundary conditions at the free surface. These boundary conditions require the solution to be a fairly complex boundary value problem, however, it is cleverly solved by a superposition of solutions in the following manner. The tangential stress at the free surface is made to vanish by the addition of an image dislocation "above" the free surface. This last superposition is commonly referred to as the Boussinesq problem. The strength of the Boussinesq load is such to cancel the normal stress on the free surface which is doubled by the addition of the image source. Using the Volterra relations, the displacement field at a point Q in a semi-infinite medium is then given by

$$u_k(Q) = \frac{1}{8\pi\mu} \iint_{\Sigma} \Delta u_i(P) W_{ij}^k(P,Q) \nu_j d\Sigma \, . \qquad (2.2)$$

Comparison of (2.1) and (2.2) shows that only the values of the kernels are changed by the imposed boundary conditions. The kernels of (2.2), W_{ij}^k, are the set of Green's functions found from the superposition of solutions which satisfy these half-space boundary conditions.

Steketee (1958a) gives the exact form of one of these functions, W^k_{12}, which is all that is necessary to approximate a vertical strike slip fault. Chinnery (1961, 1963, 1965) took the general expression (2.2) and derived an exact analytical form of the displacement and stress fields on the surface of a semi-infinite medium for an internal rectangularly-shaped dislocation surface modeling a vertical strike slip (transcurrent) fault. In performing these calculations, Chinnery assumed that the dislocation discontinuity was constant over the entire fault, and he also assumed that the Lamé parameters for the solid were equal so that the integration could be carried out exactly. Thus, the elastic medium for which this theory is applicable is one in which the Poisson ratio is constant at 0.25. Steketee (1958a) showed, however, that (2.2) is valid where $\Delta u_i(P)$ takes any form (Somigliana dislocation) provided that the tensile forces across the dislocation surface sum to zero.

Maruyama (1964) has derived the remaining five sets of Green's functions needed in the solution of an arbitrary dislocation problem. He further gives explicit, analytic solutions for the displacement field at the free surface due to constant finite dislocations on rectangular surfaces. The dislocations considered are those only along

single primary axes. The examples that he presents include cases for which the dislocation surface, Σ, is both perpendicular and parallel to the free surface.

Maruyama (1963) and Burridge and Knopoff (1964) showed that the displacement fields produced by a dislocation on a mathematical description of a dislocation fault surface is equivalent to that produced by a suitable distribution of forces on the fault surface acting as if there was no fault present. Utilization of this fact makes possible the use of work in mathematical elasticity theory done much earlier than Steketee's (1958a) work. Notable in this early literature is that by Mindlin (1936) who treated the static problem of a single force acting in a homogenous half-space. Mindlin and Cheng (1950) give explicit expressions for the displacement and stress fields due to point forces and double forces acting in an elastic half-space. Maruyama (1964) gives a short summary of the early literature in Japan and elsewhere on this subject. This includes work done by Sezawa (1929), Honda and Miura (1935), Whipple (1936), Soeda (1944) and Yamakawa (1955). Press (1965) showed that the kernels of (2.2) could be derived in a straightforward manner from the results of Mindlin and Cheng (1950). Press obtained the same results for a vertical strike slip fault as Chinnery had done

previously, and obtained the same results for a vertical dip slip fault as Maruyama (1964) derived. In this paper, Press (1965) added the analytic expressions for tilts and strains for these particular fault orientations. Savage and Hastie (1966) used the theory given by Maruyama (1964) to calculate the vertical displacements induced by dislocations on fault surfaces that could have components of dip other than in a direction perpendicular to the free surface. This led to the ability to model more geologically realistic faults.

Mansinha and Smylie (1971) completed the derivation of the displacement fields due to buried dislocations on finite rectangular surfaces. These authors give the complete closed form, indefinite integral expressions for the entire displacement fields, both at the free surface and at any depth in the elastic half-space, due to a rectangular dislocation surface that can be arbitrarily inclined. The fields are presented in such a form that they are readily evaluated numerically on the computer and involve only simple algebraic and trigonometric functions. However, these authors do not give the formulas for the strain and tilt fields arising from a dislocation across an arbitrarily inclined surface. These strain and tilt fields can be easily obtained from differentiation of the

displacement fields. Appendix 1 of this thesis gives the results of this differentiation.

Chinnery and Petrak (1968) extended the work of Chinnery (1961) by considering a model of a vertical strike slip fault on which the dislocation uniformly and smoothly goes to zero near the edges of the dislocation surface. This variation was chosen so as to remove the stress singularity that was occurring at the edge of the fault surface in the original work. Except in extreme cases, the tapering of the dislocation near the edges of the surface had little effect on the overall displacement fields calculated on the surface.

Ben-Menahem and Singh (1963a) and Ben-Menahem and Gillon (1970) computed the integral expressions for the displacement field, both dynamic and static, at the free surface for a model of a vertical strike slip fault and a vertical dip slip fault for a medium which contains a layer of arbitrary thickness over a uniform half-space. These authors point out that due to the complexity of the problem, the use of the Galerkin vectors for elastic problems involving more than one layer over a half-space would be extremely difficult. These authors suggested the use of a method employing Hansen's eigenvectors in obtaining the static response of a multilayered homogenous

half-space. McGinley (1969) and Sato (1971) achieved much the same results as these authors by the superposition of several half-space Green's functions solutions off-set in such a way as to represent a layered half-space. Braslau and Lieber (1968) solved the static linearly elastic problem of a concentrated vertical Volterra dislocation in a layer over a half-space. They made use of a special displacement function which they called a modified Galerkin vector to give the solution in a form which must be evaluated numerically. Singh (1970, 1971) has applied the Thomson-Haskell matrix propagation method (Thomson, 1950; Haskell, 1953) to solve the problem of static deformation in a multilayered elastic half-space. He obtains source functions for the six elementary dislocations that were given by Steketee (1958a). Explicit integral expressions are given for the surface displacements for a vertical strike slip and vertical dip slip fault when these faults can be represented by concentrated or point sources. Extension to finite size sources is given as another integration involving the dislocation surface. Recently Chinnery and Jovanovich (1972) have calculated the displacement field due to a vertical strike-slip fault of infinite length for an earth model consisting of two layers of arbitrary thickness and

rigidity over a half-space. Their expressions are given in series form so that no further integration is necessary. On the basis of this model, they conclude (and thus agree with McGinley (1969)) that the presence of a low rigidity layer would have a very strong (amplifying) effect on the observed displacements and strains in the far field.

Ben-Menahem and Singh (1968b) treated in detail the problem of deformation of a uniform non-gravitating sphere due to internal Volterra type dislocations of arbitrary orientation and depth. This work was subsequently expanded (Ben-Menahem et al., 1969, 1970; Singh and Ben-Menahem, 1969; Ben-Menahem and Singh, 1970; Wason and Singh, 1972) to include the computations for the displacement and strain fields everywhere on the surface of a homogenous sphere induced by an internal dipolar source of finite size. The results for a sphere were shown to be quite different than that expected in the far-field half-space problem.

Stress Pulse Theory. This approach has seen limited use in explaining elastostatic phenomenon. Kasahara (1957) devised this method to model the mechanism of an earthquake as a distribution of stresses or strains imposed on an underground plane. When the conditions of elastic equilibrium are satisfied, the deformations at the surface can be calculated. He models an infinite strike-slip

fault with a zone of constant stress extending to a given depth. The faulting occurs by the liberation of this initially applied shear stress. Horizontal displacements were calculated for various depth extensions and comparisons were made to actual faults. By examining the diminution of horizontal displacement with distance, the depth of extension of this constant stress zone is determined. This mechanism is extended in a second paper (Kasahara, 1959) to include non-vertical strike-slip faults. The static mechanism presented by Kasahara is analogous to the stress pulse problems encountered in dynamical formulations of seismic sources. Minster (1974) describes the mathematical nuances of this approach.

Stress Relaxation Theory. A third method of determining the static deformation from a model of an earthquake is obtained through an entirely different approach to the theoretical problem. The methods considered thus far are all based on relations in which conditions on various boundaries are imposed (boundary-value problems). Archambeau (1964, 1968) has proposed an alternative mechanism of describing the processes which accompany the occurrence of earthquakes -- that of material failure. This theory is devised in the context of an initial-value problem in that a medium is assumed to be initially in some prestressed state. Deformation in the medium is

caused by introducing some surface, or volume, within the medium where the material fails. This failure is accomplished by making a significant reduction in the shear tractions across the failure surface. The media then responds by "relaxing" to a new equilibrium state by radiating the energy released from the local reduction in strain energy in the source region. This theory has been very successful in the dynamical regime, most notably in the prediction of far-field radiation patterns from earthquakes and explosions accompanied by tectonic release (Archambeau and Sammis, 1970; Lambert et al., 1972; Archambeau, 1972). Because of the theoretical complexities, this source formulation has not yet been directly applied to near-field static deformation problems.

Minster (1974) has discussed from a mathematical point of view in some detail the similarities and differences between the various formulations of the earthquake processes. Although his approach is mainly based on dynamical considerations, he shows that in the static limit the general representation of the stress relaxation and stress pulse problems reduce to the displacement field as given by a generalized Somigliana dislocation along a surface of shear displacement discontinuity. This same proof was attempted by McGinley (1969), but the arguments presented by Minster (1974) are much more complete.

Therefore, we may express the source in terms of a Somigliana dislocation without loss of equivalency from the other source descriptions. An approximation to this Somigliana source will be adopted throughout this thesis.

Numerical Analogue. An altogether different approach to solving the forward problem for dislocations in an elastic half-space is afforded through the use of the finite element numerical technique. Use of this technique, which usually requires a large computing capability, enables solutions to be found to problems involving heterogenities, both later and vertical, and anisotropy just as easily as those involving a uniform homogenous, isotropic half-space. The mechanics of this method have been described extensively in the engineering literature (Martin, 1966; Przemienicki, 1968; Jenkins, 1969; Zienkiewicz, 1971). In this technique, the elastic half-space continuum is divided into geometric elements which are inter-connected only at a finite number of nodal points. It is at these nodal points that displacements, stresses, or forces can be imposed on the system. Concurrently, stresses and displacements at a distance removed from these disturbances can only be measured at these nodal points. The solution to the system of simultaneous equations generated by a disturbance imposed on a given node is constrained by the boundary conditions relevant to the problem and is

solved numerically. Jungels (1973) gives a description of the adaptation of this method to the modeling of dislocation fault surfaces. The reader is referred to this work for a summary of the intricacies of this numerical method.

Jungels (1973) and Jungels and Frazier (1973) make a positive comparison between the calculated static displacement field due to a dislocation in a uniform homogenous elastic half-space calculated by the finite element method and by the conventional exact Green's functions techniques. Although this author had at his disposal a numerical code which would allow only the modeling of plane strain problems, i.e., faults of infinite length, more recent finite element numerical codes can accommodate problems involving finite dimensions in all directions. The great advantage of this method in calculating displacement and strain fields from models of earthquakes is the ability to vary the elastic properties of the medium both over the fault surface and the source to observer path. This technique can be limited, however, by the shear size of computer storage necessary to solve a problem in which the continuum must be very finely sampled in order to accurately approximate the continuum for the order of the disturbance being modeled.

2.3 Application of the Forward Problem toward the Explanation of Observed Static Data.

As is obvious from the preceding discussion, much progress has been made toward the static modeling of the earthquake source. The state-of-the-art is such that now an accurate description of the static processes accompanying faulting can be investigated. However, the inverse problem now remains. As the facility for calculating the displacement and strain fields from fault models became more sophisticated, a wider range of data came under scrutiny in trying to infer some information about the various parameters which affect the faulting process. The earliest attempt to extract source information from static data was applied to differential horizontal displacements measured near long vertical strike-slip faults. Kasahara (1957, 1959), Chinnery (1961), and Chinnery and Petrak (1968) tried to infer the depth and distribution with depth of dislocation faulting by fitting the rate of fall-off of horizontal displacements measured parallel to the fault strike as a function of distance away from the surface expression of the fault. A trial and error method was used to fit the data and to try to exclude possible faulting models. Press (1965) and Press and Jackson (1965) used Press' calculations to model the close-in vertical movements associated with the 1964 Alaskan earthquake.

These movements were modeled with a vertical dip-slip fault and an indication was sought as to the depth of faulting. A comparison of the calculated and observed far-field residual strain steps was also undertaken. Singh and Ben-Menahem (1969) attempted to fit the same strain observations using their method for taking into account the earth's curvature. In both these studies, no attempt was made to systematically vary the source parameters to achieve the best fit to the data.

As displacement data for large earthquakes became more abundant and reliable, it became apparent that the simple fault models having a constant dislocation over the entire fault surface could not adequately represent the observations. Stauder and Bollinger (1966) first proposed that differential slip on the fault surface might provide a more realistic model to better fit the data from the 1964 Alaskan earthquake. They approximated the differential movement by allowing the displacement on the fault, Δu, to vary piecewise along the direction of the slip. To do this, the total fault plane was taken to be a sum of the individual fault surface rectangles, each being weighted separately. Unfortunately, these authors used a rather simple source model representation in that it had differential movement only on a horizontal fault parallel to the surface. Furthermore, they gave no indication as to how

they arrived at their final model. One would guess that they used the trial and error method.

Savage and Hastie (1969) and Hastie and Savage (1970) have described a quasi-inversion process to be applied to the fitting of earthquake static displacement data using the dislocation models for an arbitrarily oriented finite fault surface imbedded in a homogenous half-space. In these studies, these authors swept through predetermined sets of sensitive fault parameters -- fault width, dip angle, depth, and slip -- calculating the degree of fit to all the data for each model tested. The model which best fit the data in a least-squares sense was termed the optimum model. These calculations seem to closely coincide with the Monte Carlo techniques used to find acceptable models of the radial distributions of the elastic parameters within the earth as described by Press (1968, 1970, 1972). In these cases a reasonable fit to the data was obtained, especially in the case for the Fairview, Nevada earthquake. Fitch and Scholtz (1971) later extended this work to some degree. However, the dislocation model used in these cases was highly idealized in that it was restricted to the Volterra type dislocation in which the slip was constant over the entire dislocation surface.

2.4 Construction of the Pseudo-Somigliana Dislocation Static Model.

Since it has been shown that the fault geometries can be more complicated than just plane rectangular surfaces, some means must be derived to allow in our mathematical representation of the faulting process for these complications. Complications to the simple models can occur in at least two ways. The first complication is that we wish to be able to allow the dislocation to take on arbitrary values as a function of position over the fault surface. Secondly, the fault surface may not be a single rectangular plane. Both of these complications can easily be represented approximately by discretizing the dislocation surface. That is, we want to approximate a curved fault surface by a series of planar surfaces juxaposed in such a manner as to approximate the curvature of the surface to be matched. Curvature, or splaying, could be thus modeled in any direction. An example of matching curvature in the horizontal direction could be envisioned by a model of the San Andreas fault which includes the region of the bend in southern California. Here a series of plane vertical rectangular surfaces could be concatenated horizontally to match the observed curvature. Similarly, a dipping thrust fault in which the dip varies with depth could be approximated by a series of rectangular sheets positioned vertically to make a continuous surface in which the dip could

change discontinuously between fault elements. Examples of modeling dipping thrust faults in this manner is given in later chapters.

With this same scheme, the dislocation could be allowed to differ on each of the surface elements which comprise the total dislocation surface. Restriction on the variance of the source parameters from one surface element to the next would have to be imposed to keep the problem physical.

2.5 Linearization of the Forward Static Problem.

The net displacement or strain field at the surface, or at any point off the dislocation surface could be calculated separately for each of the individual segments using one of the forward problem formulations discussed earlier in this chapter. The total elastostatic field at a particular observation point would be a simple sum of the individual contributions from each of the comprising elements.

We wish to pose the problem in such a way as to be able to write down a succint relationship between the values of the source parameters and the data functionals which we compute from the forward problem calculations. Suppose that we calculate the values of the elastostatic field at a single point exterior to the dislocation surface of our chosen fault model system which is made up of

M different variously-oriented dislocation surface elements. Consider that the elastostatic field can be described by N field variables, preferably those for which we can observe in the field following an earthquake. Suppose that there are L source parameters which can be linearly related to the elastostatic field through the forward problem formulations. Then this relationship is given through the system of linear equations

$$\sum_{j=i}^{L\cdot M} A_{ij} m_j = d_i \qquad \text{for } i = 1,N. \qquad (2.3)$$

In these sets of equations d_i are the calculated elastostatic field functional values, m_j are the values of the linear model source parameters, and the coefficients A_{ij} are the elastic media response of a particular data functional due to a particular fault surface element having a unitary source strength for the linear parameters. These coefficients are in general a function of position. If we treat the components of m_j and d_i as elements of a column and row vector respectively and if we put the coefficients, A_{ij}, in standard matrix form where the matrix has L·M columns and N rows, we can express (2.3) in the following

matrix notation,

$$\mathbf{Am=d} \ . \tag{2.4}$$

The model components of **m** are contained in the vector space $E^{L\cdot M}$ and the data functional components are contained within the vector space E^{N}. The matrix, **A**, can be considered a vector operator which maps $E^{L\cdot M}$ into E^{N}.

We have been careful in this construction to limit ourselves to problems where the source parameters in the space $E^{L\cdot M}$ can be linearly related to the calculated elastostatic field functionals in space E^{N}. This strictly linear relation is valid for only a few source parameters in special instances. If the forward problem is to be solved by the analytic closed form Green's function solutions, for example equation (2.2), then we have to impose the Volterra restriction

$$\Delta u_i(P) \ = \ \text{constant}.$$

With this restriction we can write

$$u_k(Q) \ = \ \frac{\Delta u_i}{8\pi\mu} \iint_{\Sigma} w_{ij}^{k}(P,Q)\nu_j d\Sigma \ ,$$

and the problem is now linear with respect to slip in the

ith direction on the individual dislocation surfaces. In general, the solution cannot be so easily linearized with respect to other parameters which characterize the dislocation source-fault length, dip angle, depth, position, etc.. An examination of the forward equations given by Mansinha and Smylie (1971) is convincing with this respect. Fortunately, by numerically evaluating these expressions, we can show that they are <u>locally</u> linear. The extent of the locally linear domain varies from source parameters to source parameter and also with the absolute value of the source parameter. If sufficient care can be paid to these details, the problem can be approximately linearized for all the source parameters listed above. The linearization can be accomplished in the following simple way.

The degree of linearity or non-linearity of the forward problem functionals for the various source parameters will be model dependent, that is, it will vary from source model to source model. If we wish to describe the linear domain in a field about some chosen model, $\mathbf{m}_1$, we choose some other source model, $\mathbf{m}_2$, "near" $\mathbf{m}_1$ such that the following equation can be written

$$\mathbf{A}\,\delta\mathbf{m} = \delta\mathbf{d} + O[|\mathbf{m}_2 - \mathbf{m}_1|^2]. \qquad (2.5)$$

The following definitions have been applied:

$$\delta \mathbf{m} = \mathbf{m}_2 - \mathbf{m}_1 \tag{2.6}$$

$$\delta \mathbf{d} = \mathbf{d}(\mathbf{m}_2) - \mathbf{d}(\mathbf{m}_1) \, . \tag{2.7}$$

$\mathbf{d}(\mathbf{m}_i)$ is the elastostatic field for a particular source model $\mathbf{m}_i$. The problem is linearized only if $\delta \mathbf{m}$ is sufficiently small for equation (2.5) to hold. The conditions for linearity discussed here are equivalent to requiring the forward problem functionals to be Fréchet differentiable with respect to the source parameters.

If we calculate the forward problem for a source model description which we think will reasonably approximate the observed static field functionals, call this model $\mathbf{m}_s$, then for small perturbations about this model, $\delta \mathbf{m}_s$, an approximate linear relationship between the two vector spaces is established. This is to say that the coefficients of A_{ij} are linear. We note here that in general, the coefficients of A_{ij} are not independent of the model $\mathbf{m}_s$. Indeed, their dependence is a measure of the non-linearity of the operator coefficients in the region of the model space being sampled by the test model $\mathbf{m}_s$. The perturbations, $\delta \mathbf{m}_s$, must remain small in the sense that they are approximately linear throughout this region.

In our matrix notation the forward problem is now written

$$\mathbf{A}\,\delta\mathbf{m}_s = \delta\mathbf{d}_s \,. \tag{2.8}$$

2.6 Derivation of the Stochastic Inversion Operators. Introduction. This section addresses the problem of obtaining the best estimate of the source parameters characterizing a fault model given a suite of observations which can be linearly related to the faulting process. The problem here follows closely that encountered in the studies regarding the estimation of the radial distribution of velocity and density within the earth. In this area of research, much theoretical progress has been made in the last six years in the treatment of inversion schemes to estimate these distributions. Perhaps the most successful and certainly the most elegant of these schemes falls in the general category of stochastic inversion theory. This theory, which will be applied to the treatment of elastostatic problems in this thesis, attempts to give the best estimate of a discretized approximation to the continuous faulting process when a limited amount of data is obtainable. As pointed out by Jordan (1972), the inverse problem when posed in this manner usually has no unique solution. However, the solution that is obtained is unique in certain respects, as will be discussed later.

Furthermore, the stochastic approach allows for the inclusion of inaccuracies in the estimation of the elastostatic field observations. How these inaccuracies affect our model estimations will be fully explored in the chapters devoted to the application of this theory.

The fundamentals of the theory for the solution of the underconstrained linear inverse problem for data that contain certain amounts of "noise" have been presented by Backus and Gilbert (1967, 1968, 1969, 1970). Jordan and Minster (1971) and Jordan (1972) incorporated portions of the Backus-Gilbert theory with the purely stochastic theory of Franklin (1970) to present a quite complete approach to the solution of this type of problem. The theory as applied here to static problems is essentially that due to Jordan (1972), and an attempt has been made to follow his notation throughout this thesis. Sophisticated discussions as to the validity of this type of inverse and the mapping functions of the operators are given in this reference. The derivation of the stochastic inversion operators below are given only in the context as to how they apply to the elastostatic problem. In the derivations, for reasons of simplicity the notation used is for a linear problem. If applied to non-linear problems that have been linearized in the procedure discussed above, the difference vectors defined in (2.6) and (2.7) are

merely substituted for the true model and elastostatic field vectors.

Derivation. Consider the problem of determining some M-dimensional vector model, **m**, contained in the space E^M, given a N-dimensional elastostatic field vector, **d**, in the space E^N. The elastostatic field values are related to by the system of linear equations

$$\sum_{j=1}^{M} A_{ij} m_j = d_i \qquad i = 1, N \; . \tag{2.9}$$

In matrix notation

$$\mathbf{A}\,\mathbf{m} = \mathbf{d} \quad , \tag{2.10}$$

where the operator **A** solves the forward problem for each of the N elastostatic field values contained in **d** by mapping E^M into E^N. Thus for every model **m** there exists some unique determination of **d** where

$$\mathbf{d} = \mathbf{d}(\mathbf{m}) \; . \tag{2.11}$$

If we take the actual field observations which are measured following the occurrence of an earthquake to be in vector form, $\mathbf{d}_0$, and these measurements are made perfectly with no

inaccuracies, then

$$\mathbf{d}_0 = \mathbf{d}(\mathbf{m}) \ . \tag{2.12}$$

Assuming, of course, that the formulation of the forward problem will exactly determine the elastostatic field values. However, if there are any inaccuracies in the observed field values, then these observed values, $\mathbf{d}_0$, can be written as a combination of the projected field values plus some measure of the uncertainty in these observations,

$$\mathbf{d}_0 = \mathbf{d}(\mathbf{m}) + \mathbf{n} \ , \tag{2.13}$$

or by substitution from (2.10)

$$\mathbf{A}\,\mathbf{m} = \mathbf{d}_0 + \mathbf{n} \ . \tag{2.14}$$

Here $\mathbf{n}$ is a vector containing the components of the "noise" in the observed field data. We assume that this noise is randomly distributed in a Gaussian fashion and that any bias to the data is removed before the noise is estimated. Each component, d_{0_i}, is assumed to be the mean of a Gaussian random variable with variance, σ_i^2. We can define a diagonal variance operator, $\mathbf{C}_{nn}$, to be

$$C_{nn} = \begin{bmatrix} \sigma_1^2 & . & . & . & 0 \\ . & \sigma_2^2 & & & . \\ . & & . & & . \\ . & & & . & . \\ . & & & . & . \\ 0 & . & . & . & \sigma_N^2 \end{bmatrix} , \qquad (2.15)$$

where σ_i^2 is the estimated variance of the ith data value. In assuming this diagonal form, we are implicitly assuming that there is no co-variance between data.

Since the only information that we have about $\mathbf{m}$ is contained in (2.14), we know nothing about the components of $\mathbf{m}$ which lie outside the space $\mathbf{R} \subseteq E^M$ which is spanned by the vectors $\{a_i : i=1,N\}$. It is reasonable to require that our estimate of $\mathbf{m}$, call it $\tilde{\mathbf{m}}$, lie totally within the subspace $\mathbf{R}$; then we can assign a non-zero value to only those components for which we have information. Under this restriction, we can write

$$\tilde{\mathbf{m}} = \mathbf{A}^* \mathbf{b} \qquad (2.16)$$

for some vector $\mathbf{b}$ contained in the vector data space E^N. In this last equation, we are using the notation $\mathbf{A}^*$ to represent the transpose of the matrix $\mathbf{A}$. This convention will be used throughout this thesis. To select an optimal $\mathbf{b}$, call this $\tilde{\mathbf{b}}$, we wish to minimize a suitable quadratic

measure of the errors involved in this estimation. We choose to minimize some weighted sum of two measures of the errors involved in this problem. This weighted sum can be parameterized by a trade-off curve between these two errors, with the position along this curve used as the parametric factor. Specifically, we want to minimize

$$\varepsilon^2(\theta,\mathbf{b}) = \varepsilon_1^2(\mathbf{b}) \cos(\theta) + \varepsilon_2^2(\mathbf{b}) \sin(\theta) \quad , \tag{2.17}$$

where

$$\varepsilon_1^2(\mathbf{b}) = ||\mathbf{m} - \mathbf{A}^*\mathbf{b}||^2 \quad , \tag{2.18}$$

and

$$\varepsilon_2^2(\mathbf{b}) = \mathbf{b}^* \mathbf{C}_{nn} \mathbf{b} \quad . \tag{2.19}$$

The first measure of error, $\varepsilon_1^2(\mathbf{b})$, is the square of the Euclidian norm, defined by

$$||\mathbf{X}||^2 = \sum_{i=1}^{M} x_i^2 \quad ,$$

of the difference between our estimate of the model, $\tilde{\mathbf{m}}$, and the actual vector we are estimating. This quantity decreases as we more closely approximate $\mathbf{m}$. The second

measure of error associated with $\tilde{\mathbf{b}}$ arises from uncertainty in the components of $\mathbf{d}_0$. This quantity decreases as our estimate becomes more reliable. The parameterization angle, θ, is allowed to vary on the interval $[0,\pi/2]$, so that at $\theta = \pi/2$, $\varepsilon_2^2(\mathbf{b})$ is minimized, indicating maximum reliability of the model. At $\theta = 0$, $\varepsilon_1^2(\mathbf{b})$ is minimized, indicating maximum accuracy in the estimation of the model.

We note here that these two errors are measured with two different norms, each in the model space. We must establish some common norm on each of these errors so that the parameterization of the sum of these errors can be accomplished. This normalization is performed through the introduction of a correlation operator, $\mathbf{W}$. This correlation operator can be thought of simply in terms of a weighting function for the various model components. The norm of this operator is fixed so that at the critical point on the trade-off curve between the two types of errors, at $\theta = \pi/4$, the absolute value of the two errors are equal.

For the present, we assume that the correlation operator, $\mathbf{W}$, is the idemfactor, $\mathbf{I}$, so that this effect can be ignored in our minimization calculations. The results of this minimization then will be generalized to include an arbitrary correlation operator.

In order to minimize $\varepsilon^2(\theta,\mathbf{b})$ given in equation (2.17), we take $\delta\mathbf{b}$ to be a small arbitrary perturbation of $\mathbf{b}$. To first order in $\delta\mathbf{b}$ we can write

$$\delta\varepsilon^2(\theta,\mathbf{b}) = \varepsilon^2(\theta, \mathbf{b}+ \delta\mathbf{b}) - \varepsilon^2(\theta,\mathbf{b}) \quad .$$

Performing this first order perturbation on equation (2.17) we find that

$$\delta\varepsilon^2(\theta,\mathbf{b}) = 2[\mathbf{b}\mathbf{A}\mathbf{A}^* - \mathbf{m}\mathbf{A}^*]\delta\mathbf{b}\cos(\theta) + 2\,\mathbf{b}\mathbf{C}_{nn}\delta\mathbf{b}\sin(\theta) \quad .$$

In order to minimize $\varepsilon^2(\theta,\mathbf{b})$, we set $\delta\varepsilon(\theta,\mathbf{b}) = 0$. When this is done, we see that $\delta\mathbf{b}$ truly is an arbitrary perturbation, and $\varepsilon^2(\theta,\mathbf{b})$ will be stationary if and only if

$$(\mathbf{A}\mathbf{A}^* + \tan(\theta)\,\mathbf{C}_{nn})\mathbf{b} = \mathbf{A}\mathbf{m} \quad . \tag{2.20}$$

It can be shown (Jordan, 1972) that this stationary point is a unique minimum, and the vector, $\mathbf{b}$, which satisfies this condition is our optimum vector, $\tilde{\mathbf{b}}$.

If $\mathbf{C}_{nn}$ is non-singular, that is, each $\sigma_1^2 \neq 0$, and $\theta > 0$, then the matrix $(\mathbf{A}\mathbf{A}^* + \tan(\theta)\,\mathbf{C}_{nn})$ is non-singular and

$$\tilde{\mathbf{b}} = (\mathbf{A}\mathbf{A}^* + \tan(\theta)\,\mathbf{C}_{nn})^{-1}\mathbf{A}\mathbf{m} \quad . \tag{2.21}$$

In this last equation, $\mathbf{m}$ is unknown but by substituting from equation (2.10) we get

$$\tilde{\mathbf{b}} = (\mathbf{A}\mathbf{A}^* + \tan(\theta)\, \mathbf{C}_{nn})^{-1}\, \mathbf{d}_0 \ . \tag{2.22}$$

Substituting this optimal value of $\mathbf{b}$ into equation (2.16) we see that the optimal estimate of the model for a fixed value of θ will be given by

$$\tilde{\mathbf{m}} = \mathbf{A}^* (\mathbf{A}\mathbf{A}^* + \tan(\theta)\, \mathbf{C}_{nn})^{-1}\, \mathbf{d}_0 \ . \tag{2.23}$$

In the above results all components of $\mathbf{m}$ are equally weighted with the identity operator. A more general weighting can be introduced by considering a set $\{W_j ; j=1,M\}$ of non-zero positive weights for the model components. Let us define this weighting, or correlation matrix, in the following manner,

$$\mathbf{W} = \begin{bmatrix} W_1^2 & . & . & . & . & 0 \\ . & W_2^2 & & & & . \\ . & & . & & & . \\ . & & & . & & . \\ . & & & & . & . \\ 0 & . & . & . & . & W_M^2 \end{bmatrix} \ .$$

This leads us to define a normalized elastic media response operator

$$\mathbf{A}' = \mathbf{A}\mathbf{W} \quad . \tag{2.24}$$

With this normalized definition, equation (2.10) is now written

$$\mathbf{A}'\mathbf{W}^{-1}\mathbf{m} = \mathbf{d}_0 \quad . \tag{2.25}$$

Following the same procedure as before, we require

$$\tilde{\mathbf{m}} = \mathbf{A}'^{*}\mathbf{b} \quad , \tag{2.26}$$

and minimize

$$\varepsilon_W^2(\theta,\mathbf{b}) = ||\mathbf{m} - \mathbf{A}'^{*}\mathbf{b}||_W^2 \cos(\theta) + \mathbf{b}^{*}\mathbf{C}_{nn}\mathbf{b} \sin(\theta) \quad ,$$

where $||\cdot||_W$ is the weighted norm defined by

$$||\mathbf{Z}||_W^2 = \mathbf{Z}^{*}\mathbf{W}^{-1}\mathbf{Z} = \sum_i \left(\frac{z_i}{w_i}\right)^2 \quad .$$

This weighted norm, of course, reduces to the Euclidian norm if $W_i = 1$ for all $i = 1,M$. The minimization of $\varepsilon_W^2(\theta,\mathbf{b})$ with respect to a variation of $\mathbf{b}$ procedes as before. The results are

$$\tilde{\mathbf{m}} = \mathbf{W}\mathbf{A}^{*}(\mathbf{A}\mathbf{W}\mathbf{A}^{*} + \tan(\theta)\, \mathbf{C}_{nn})^{-1}\, \mathbf{d}_0 \quad . \tag{2.27}$$

Now since there are uncertainties in the observed elastostatic field, the best estimate of the model, $\tilde{\mathbf{m}}$, is some filtered average of the true model, $\mathbf{m}$, given by

$$\tilde{\mathbf{m}} = \mathbf{R}\,\mathbf{m} \quad . \tag{2.28}$$

This averaging operator, which contains the response kernels for the elements of $\mathbf{m}$ can easily be found by substituting for $\mathbf{d}_0$ in equation (2.25). Performing this substitution in equation (2.27) we obtain

$$\tilde{\mathbf{m}} = \mathbf{W}\mathbf{A}^{*}(\mathbf{A}\mathbf{W}\mathbf{A}^{*} + \tan(\theta)\,\mathbf{C}_{nn})^{-1}\mathbf{A}\,\mathbf{m} \ ,$$

or by inspection from equation (2.28)

$$\mathbf{R} = \mathbf{W}\mathbf{A}^{*}(\mathbf{A}\mathbf{W}\mathbf{A}^{*} + \tan(\theta)\,\mathbf{C}_{nn})^{-1}\mathbf{A} \quad . \tag{2.29}$$

Individual rows of this operator contain the averaging of the estimated values of the individual model components with respect to the other model components. This averaging is taking place in a sense that the estimation of the ith model component is actually the true value of this component "convolved" in the model space with the function defined on the model space by the components of the ith row of the averaging operator. If a particular model component is perfectly determined, say the ith value, that is, its value is perfectly resolvable, then $R_{ii} = 1$ and all other $R_{ij} = 0$.

In the limit of infinite resolution on all model components, that is, either $\theta = 0$ or $\mathbf{C}_{nn} = 0$, the averaging operator approaches the idemfactor, $\mathbf{I}$.

By similar substitutions, we can express equation (2.19) as

$$\varepsilon_2^2(\theta,b) = \mathbf{m}^* \mathbf{V}(\theta)\, \mathbf{m} \quad , \tag{2.30}$$

where we have defined a new operator

$$\mathbf{V}(\theta) = \mathbf{W}\,\mathbf{A}^*(\mathbf{A}\mathbf{W}\,\mathbf{A}^* + \mathbf{C}_{nn}\tan(\theta))^{-1}\,\mathbf{C}_{nn}(\mathbf{A}\mathbf{W}\,\mathbf{A}^* + \mathbf{C}_{nn}\tan(\theta))^{-1}\mathbf{A}\mathbf{W} \quad . \tag{2.31}$$

This operator is termed the variance operator. Examining equation (2.30) we see that the bilinear product of this operator and the model components is a measure of the error induced from the data space, through the variance matrix $\mathbf{C}_{nn}$, into the model space. Since we are assuming that the errors exhibited in $\mathbf{C}_{nn}$ are normally distributed, we can determine the following about the errors induced from the data space due to inaccuracies in the description of the elastostatic field into inaccuracies in the estimated source model parameters. Use of this operator does not tell us the absolute inaccuracies of our estimated model

per se; instead, it can only tell us whether or not a certain perturbation in the model is resolvable to a certain degree by the data. So in practice, we have to prescribe a perturbation vector on our source model and test to see if the data can "see" this perturbation. This ability to distinguish model perturbations by the observed data will depend directly on the accuracy of the data. The more accurate the data, the smaller a model perturbation these data will be able to detect. Since we are now mapping errors in the opposite direction as that defined in equation (2.30), clearly the inverse of this operator is the projection that we desire. Since the errors are induced in directions along the eigenvectors of $\mathbf{V}(\theta)$, then we choose to take the inverse of this operator as the generalized inverse given by

$$\mathbf{V}^{\dagger}(\theta) = \sum_{i=1}^{J} \frac{1}{\lambda_i^2} \mathbf{u}_i \bullet \mathbf{u}_i^{*} \quad . \tag{2.32}$$

Here we are assuming that $\mathbf{V}(\theta)$ has a total of J non-zero eigenvalues (λ_i^2, i=1,J) with the associated eigenvectors $\mathbf{u}_i$. The notation $\mathbf{u}_i \bullet \mathbf{u}_i^{*}$ indicates an outer-product expansion between the two vectors $\mathbf{u}_i$ and $\mathbf{u}_i^{*}$. Since $\mathbf{V}^{\dagger}(\theta)$ is a generalized inverse of $\mathbf{V}(\theta)$, then the inner product of $\mathbf{V}(\theta)$ and $\mathbf{V}^{\dagger}(\theta)$ are not necessarily the identity operator

but rather some projection operator, $\mathbf{P}_v$ that is both idempotent ($\mathbf{P}_v \mathbf{P}_v = \mathbf{P}_v$) and symmetric ($\mathbf{P}_v = \mathbf{P}_v^*$).

In particular, some vector perturbation in the model space, $\mathbf{q}$, is resolvable to within a certain confidence limit, to which we can assign some confidence coefficient k(c), if the following inequality holds.

$$\underline{\mathbf{q}}^* \mathbf{V}^\dagger \mathbf{q} > k^2(c) \ . \tag{2.33}$$

For example, for the 95% confidence limit, k(c) can be found in any good statistics reference to be 1.96.

A two-dimensional geometrical argument will illustrate the use of equation (2.33). Assume that the errors induced from the data space onto the model space by the variance operator (eigenvalues of this operator) are $\sigma^2_{m_1}$ and $\sigma^2_{m_2}$. (This variance should not be confused with the data variance defined in equation (2.15)). These errors lie along the eigenvector directions, $\hat{x}_1$ and $\hat{x}_2$ respectively. Now if a vector $\mathbf{x}$ has components along these directions then the equation

$$\mathbf{x}^* \mathbf{V}^\dagger \mathbf{x} = k^2$$

can be written out

$$\frac{x_1^2}{\sigma^2_{m_1}} + \frac{x_2^2}{\sigma^2_{m_2}} = k^2 \ .$$

This is just the equation of an ellipse whose semi-major axes are $k\sigma_{m_1}$ and $k\sigma_{m_2}$. This ellipse, or hyper-ellipsoid when this argument is extended to higher dimensions, is called the confidence ellipse. The enclosure of this ellipse represents the area of unresolvable model perturbations, and the area exterior to the ellipse represents a model perturbation which is large enough to be resolvable by the data at a certain confidence limit associated with the axis parameter k. By making k larger, we are increasing the confidence limit and increasing the size of the confidence ellipse thus requiring larger model perturbations before they can be detected by the data at that confidence limit. In order to check the resolvability of a given model perturbation, we choose our value of k (say 1.96) and merely test to see if this vector protrudes the confidence ellipse. We note here that this resolvability criterion depends only on relative perturbations to the source model parameters and not on the absolute configuration of the final or optimum model that we obtain from the inversion process. Thus we have to propose a hypothetical perturbation, or a series of perturbations, judiciously chosen to explain or disclaim certain features of our model, and expose them to this testing procedure. Only on this basis can we determine the limits the model source

parameters can take and still fit the observed elastostatic field. The power of this operator becomes apparent when applied to actual problems as we shall see in later chapters.

2.7 Discussion.

In this chapter we have discussed the development of methods of obtaining an accurate representation of the forward elastostatic problem for a given description of the faulting process. We have reviewed the early uses of these forward formulations in attempting to deduce source parameters which can characterize a given event. A method was suggested by which a more complicated and arbitrary static dislocation function could be approximated with the formulations derived from simple dislocation sources. It was found that by making possible a more complex static source description some means must be used to systematically relate the observed elastostatic phenomena to the media response from the various source parameters. The stochastic inversion scheme provided an ideal means to give the best estimates to the solution for the usually underdetermined static problem. By use of this inversion scheme, we can benefit from the use and knowledge of the various operators which fall out of the derivations. These operators deal with the errors in both the observations and those in our solutions. Quantitative appraisals of the

decency of a given solution to a particular static problem become available through the use of these operators.

For the special case of $\theta = 0$, equation (2.23) is commonly known as the generalized inverse. For this case, Noble (1969, p. 143) has shown through the method of Lagrange multipliers that the generalized inverse also minimizes the norm of $\tilde{\mathbf{m}}$. We can think of this as physically giving the longest wavelength, or smoothest model solution, for a given set of data. In elastostatic problems, this property is especially valuable, since we would expect the displacement on a fault surface to locally vary in some fairly smooth fashion.

By combining all of the formalisms discussed in this chapter, we should be able to take a formidable advance in our understanding of the static processes which accompany earthquakes. The theory discussed here will be applied to data from actual earthquakes in the following chapters.

Chapter 3

A Static Dislocation Model of the 1964 Alaska Earthquake

3.1 Introduction.

The Alaska earthquake of 28 March 1964 which was centered near Prince William Sound was probably the largest seismic event in North America this century. The magnitude of this event has been estimated to be between $M_s = 8.3$ to $M_s = 8.6$. With the possible exception of the 1971 San Fernando, California earthquake, this earthquake has been the most intensely studied occurrence in the history of geophysics. The regional deformation accompanying this event involved changes in land level of unprecedented areal extent, encompassing some 200,000 km^2. The residual vertical displacements produced were measurable geodetically along a 400 km profile approximately perpendicular to the Gulf of Alaska and approximately 800 km adjacent and parallel to the coastline. Yet despite the importance that this earthquake had on the tectonic character of the affected region and the importance of the contributions that the data from this event provided toward an increased scientific understanding of the origin of earthquakes, considerable controversy still surrounds the exact source mechanism. It is hoped that the results from

this chapter will help allay some of this controversy.

3.2 Fault Representation.

Since the first studies of the 1964 Alaska earthquake, the main focal mechanism and the accompanying sense of motion have remained somewhat of a controversy primarily because of the ambiguity of the fault plane solutions based on P-wave first arrival data. The two contesting mechanisms are one having the geometry of a nearly vertical reverse fault, and the other a low angle thrust fault. Figure 3.1 shows a profile extending from the southeast to the northwest approximately bisecting the elongated area of deformation. This cross section corresponds to profile BB' shown in Figure 3.2. In Figure 3.1 we have diagrammatically represented the two possible fault plane mechanisms and their relation to the hypocenter, shown at the intersection of these two planes. The representative geometry that we choose to explain in detail the static fields which accompanied this earthquake must be in reasonable compatibility with the geometry necessary to explain the following observed or calculated entities:

1) epicenter location and hypocentral depth
2) P-wave first motion polarities and S-wave polarizations
3) aftershock distribution
4) radiation patterns of long period Love and

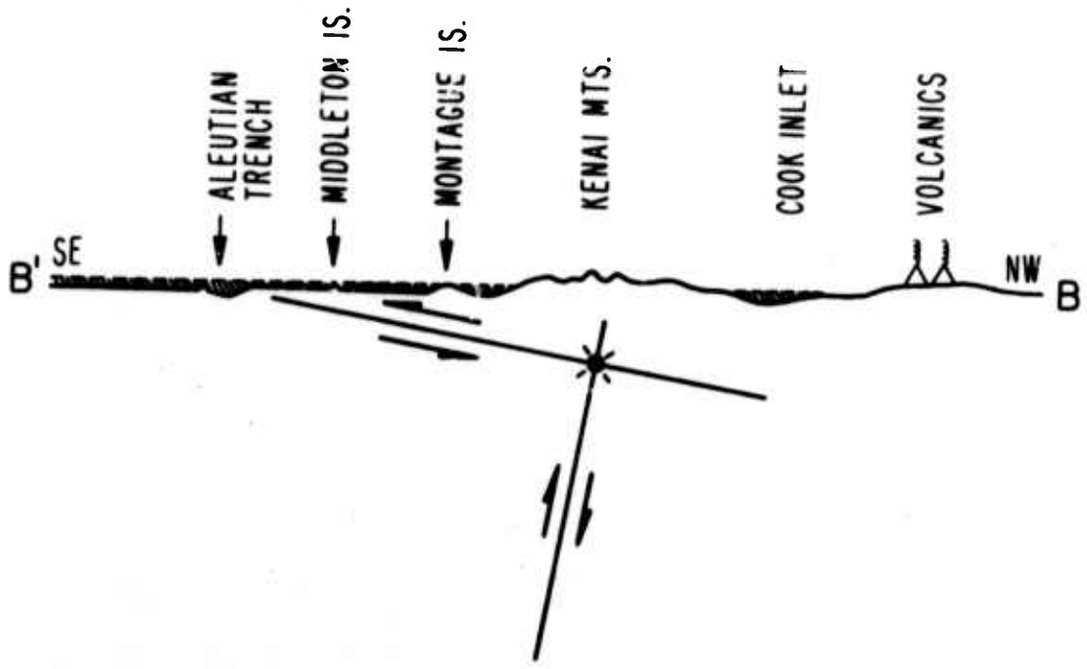

Figure 3.1. Schematic diagram of the two possible nodal planes and the relative dislocation on each. The hypocenter of the main shock is located at the intersection of the two planes.

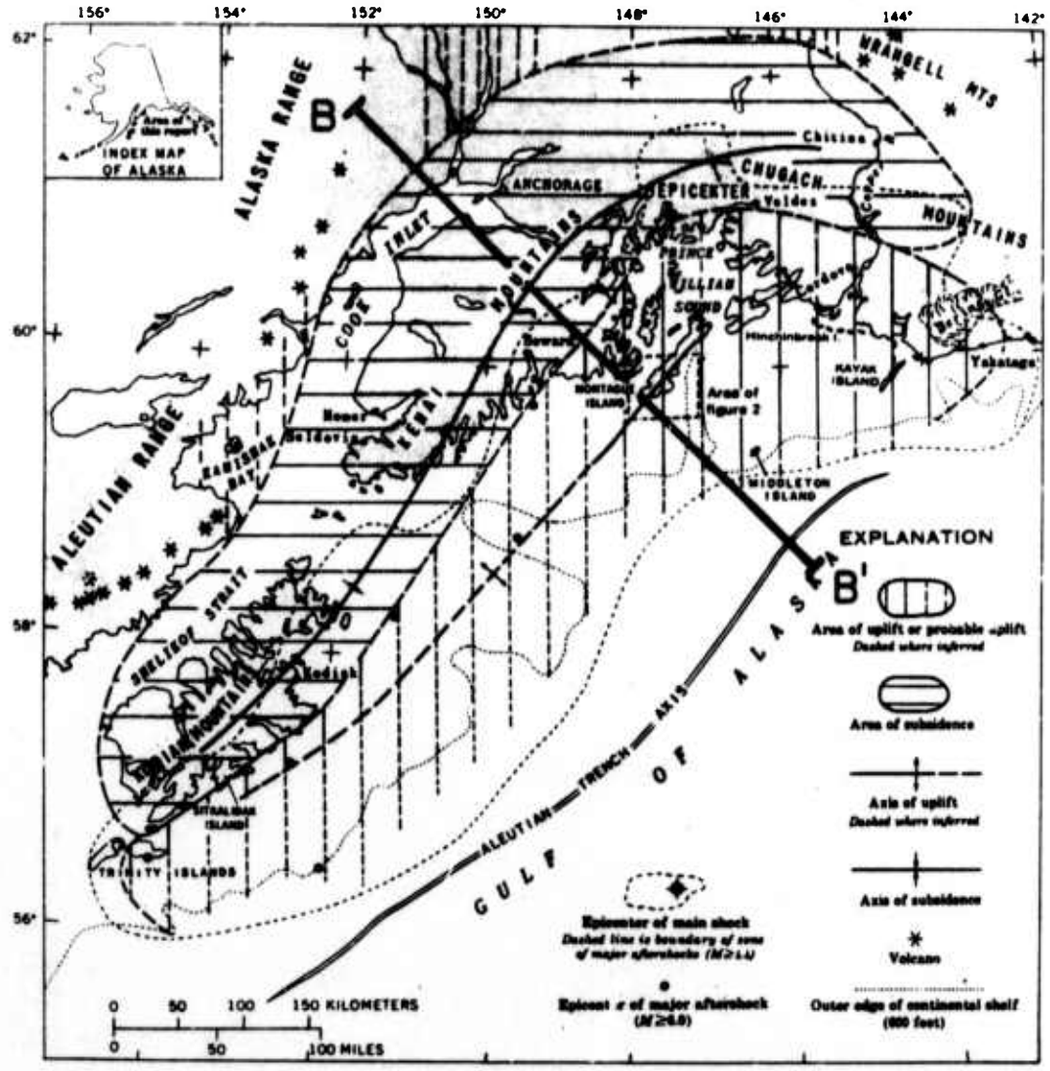

Figure 3.2. Regional deformation that accompanied the March 28, 1964, Alaska earthquake. Cross section used in this study is labeled BB'. The Patton Bay fault is indicated as the axis of uplift. Figure is from Plafker (1967).

Rayleigh waves

5) geological reasoning for faulting -- island arc implications

6) near field displacements.

We will briefly review the geophysical literature for supportive arguments to favor one or the other of the proposed mechanisms. We will then adopt a model which we think will best fit all of these criterior.

The hypocentral depth for the main event was first given to be about 20 km, and in later calculations with the inclusion of more data the depth was restricted to 33 km. (This restricted depth is the standard depth assigned a shallow event when the depth determination algorithm does not converge, or else converges to a negative depth.) No depth sensitive phases, such as pP or sP could be positively identified on records of the main shock. A reasonable assumption would be to place the depth as lying between 20 km and 50 km. The hypocenter certainly was not deep as evidenced by the large amplitude surface waves generated by this earthquake. The epicenter of the main shock was located by Sherburne et al. (1968) and von Hake and Cloud (1966) to be near the north shore of the Prince William Sound on the small peninsula separating College Fiord and Unakwik Inlet. The coordinates of the epicenter are given as 61.04° $\pm$ 0.05° north latitude and 147.73°

± 0.07° west longitude.

The focal mechanism for the first motion of this earthquake has been studied by a number of authors (Algermissen, 1964, 1965, 1966; Harding and Algermissen, 1969; Berg, 1965; Stauder and Bollinger, 1966). These studies show only one fairly well-defined nodal plane. There is some slight ambiguity in the exact orientation of this plane due to non-impulsive, or emergent P-wave first arrivals at a number of key stations, but this is a second order effect. The preferred orientation of this nodal plane is given to be strike N 62° E, dip 82° S. The definition of the second nodal plane is limited because of the almost total lack of geographical control in the station locations. Berg (1965) attempted with limited success to determine the orientation of this second nodal plane by observing a dilatation at one station, Yellowknife, Canada. The location of this station is critical in defining this second nodal plane. The orientation of this plane has been estimated to give a dip of 26° to the northeast. This unfortunate distribution of stations to the north of the epicenter precludes the identification of the nodal plane that would be present due to a low angle thrust, although the plane has been restricted by the data presented by Stauder and Bollinger (1966). These authors conclude that the second nodal plane can have a dip varying from less

than 25° to the northeast through 5° to the northwest to less than 60° to the southeast. S-wave polarization studies suffer from the same restriction in the station distribution respect. The results from the S-wave polarization angle study by Harding and Algermissen (1966) indicate that for a double couple type source on a nearly vertical fault the required motion to fit the observed S-wave polarities would be predominantly strike-slip.

One suggestion that must be kept in mind when trying to interpret the orientation of the nodal planes from first motion data is that presented by Wyss and Brune (1967). These authors suggested that the faulting which occurred over the entire segment involved a complex multiple rupture mechanism. If this mechanism is in fact the way the faulting took place, then the initial motion at the hypocenter can have little, if any, bearing on how the faulting proceeded as a whole.

One clue as to the possibility of deciding which type faulting took place is given by examining the spatial distribution of aftershocks. Algermissen et al. (1972) present just such data for over 2,000 locatable aftershocks. Special attention was given to a sub-set of this aftershock location data which were well located and contained positively identifiable depth phases. These events showed that, especially in the vicinity of Prince William Sound, the

aftershocks were shallow. In fact, approximately 62% were located at depths less than 20 km with only 1% of the events located at depths greater than 40 km. This depth distribution of aftershocks suggests that most or all of the faulting was confined within the crust and perhaps the top of the upper mantle along the continental margin. These authors depict the foci of the aftershocks located in this area under consideration as defining a plane which dips at a shallow angle (4°-6°) under the continental block. Focal mechanism studies of the aftershock by Stauder and Bollinger (1966) delineate a fault plane some 600 km in length and at least 200 km in width having an average dip of about 10°, while the main shock had a depth of focus of between 20 and 50 km and had a body wave nodal plane solution dipping between 10° and 15°.

The outer limits of the aftershock region appear to be very well defined and the region is not confined along the surface trace of the postulated steep-fault model. The aftershocks lie mainly in a broad belt roughly paralleling the continental margin mostly falling in the area of mapped or inferred major uplifting. The aftershock zone is not even approximately centered on the epicenter of the main shock.

Surface wave studies of this earthquake have been limited to long period multiple Love and Rayleigh waves due

to the tangled complexity of the large amplitude records at the WWSSN stations. With only few exceptions, the first multiples to be fully recovered have been the R4 and G4 wave trains. These signals have been analyzed in two different, but hopefully equivalent, ways. Toksöz et al. (1965) and Ben Menahem et al. (1972) used the spectral phase and amplitude equilization method while Kanamori (1970) used a time-domain analysis. For a simple point double couple source, the radiation patterns for surface waves for the two contesting fault orientations are approximately equivalent. However, if the source has some finiteness as exhibited by propagating in a given direction then assymmetries in the Love and Rayleigh wave radiation patterns are introduced. As pointed out by Savage and Hastie (1966, p. 4899-4900), the assymmetries between Love and Rayleigh wave radiation patterns will be different only if the rupture propagation is not along the null axis. If rupture does take place in a direction away from this axis then there is a possibility of distinguishing uniquely the two fault orientations. Because of differences in azimuthal coverage, Ben Menahem et al. did not detect any assymmetries in his radiation patterns while Kanamori did. Kanamori interprets this assymmetry in terms of a measured component of rupture propagation normal to the strike of the fault. His solutions favor

the low-angle thrust mechanism and his model is compatible with the long period surface waves radiation patterns for a fault dipping at about 20°.

Plafker (1965) uses his interpretation of a vast quantity of field observations in the area of deformation to argue rather forcefully for the low angle thrust mechanism. These arguments will not be repeated here but are based mainly on the large displacements in relation to the focal mechanism studies and the spatial distribution of aftershock seismicity. Plafker (1972) extends much the same arguments for a low angle thrust fault in the context of being consistent with the mechanism expected for island arc tectonics (Isacks et al., 1968; Stauder, 1968). He concludes that the earthquake occurred as shear failure on a fairly complex major low angle thrust fault, or megathrust, that dips from the vicinity of the offshore trench to beneath the continental margin. The overthrusting is interpreted in terms of elastic rebound resulting from the progressive underthrusting of the oceanic crust and mantle beneath the continental margin prior to 1964. This mechanism is consistent with Benioff's (1954) theory for oceanic trenches and associated mountain ranges.

On the basis of modeling the observed vertical displacements, Press and Jackson (1965) and Press (1965) attempted to demonstrate that the observed uplift and

subsidence could be accounted for by about 10 m of constant dip-slip motion on a vertical plane extending from a depth of about 15 km down to a depth of 150 km or more. These authors did not include in their data set all vertical displacement points available. Savage and Hastie (1966) and Hastie and Savage (1970) got better results trying to fit the same data with a low angle thrust fault with about 10 m of constant displacement over the entire surface. Savage and Hastie showed that the vertical reverse fault model geometry placed the zone of maximum subsidence too close to the zone of maximum uplift, whereas for the low angle thrust geometry, this observed lack of symmetry in the vertical displacements is approximately satisfied. Stauder and Bollinger (1966) accomplished a more realistic modeling of the displacements on a horizontal thrust fault on which differential movement on the fault surface was allowed. These authors tried to include the effects of local or subsidiary faulting on Montague Island (see Figure 3.2). The local faulting shows a dominance of vertical slip and has been described by Plafker (1965) and Grantz et al. (1964a,b). Stauder and Bollinger (1966) model this secondary fault as a constant dip-slip dislocation on a vertical surface directly beneath Montague Island.

Additionally, the low angle geometry is preferable in

describing the behavior of the observed extensive horizontal surface deformation as reported by Parkin (1966). The sense of this deformation is mainly consistent with the seaward overthrusting of the continental block. This direction of motion is especially predominant in the area between the Kenai Mountains and the offshore islands. However, we see from Figure 3.1 that we would intuitively expect the horizontal displacements to be in the opposite direction if the steeply dipping reverse faulting mechanism were adopted. Thus we have decided to adopt the low angle thrust geometry for our fault model in explaining the surface displacement data because it seems most consistent with the seismic, geodetic and geologic observations pertaining to this earthquake.

In each of these attempts in modeling the vertical displacements the formulation of a dislocation in a uniform elastic half-space was used (Green's functions solutions). Since this is a region where there is a large contrast in the juxaposed crustal types -- oceanic crust underthrusting continental crust -- this uniform elastic half-space approximation may not be appropriate. This approximation will be investigated later in this chapter. All of the above models are able to fit only the gross features of the zero-frequency data of this earthquake, not just because the earth's crust is not a uniform elastic

half-space and the slip varies continuously along the fault plane, but also because the estimates of the fault offsets were not related to the observations in a systematic fashion.

For this earthquake we will model the tectonic environment with a laterally heterogenous geologic model. The finite-element formulation will be used to compute the static response of a structural model of the crust to a unit offset imposed on a series of nodal segments representing the fault, and the inversion technique will be used to invert any free-surface statical observations to obtain the proper linear combination of these offsets which will result in a computed movement of the surface which fits the observed data to some chosen degree of accuracy. Since the finite-element formulation used in this chapter is limited to solving problems involving plane strain elasticity, any displacement profile that is to be modeled correctly must be approximately free of fault end effects and movement due to strike slip motion. The effect of assuming an infinite length fault will be discussed in a later portion of this chapter.

The structural model chosen for this study is given in Figure 3.3. The geometry is based upon that suggested by Plafker (1972) and Stanley (1966) as being the most consistent with the regional tectonic setting of the

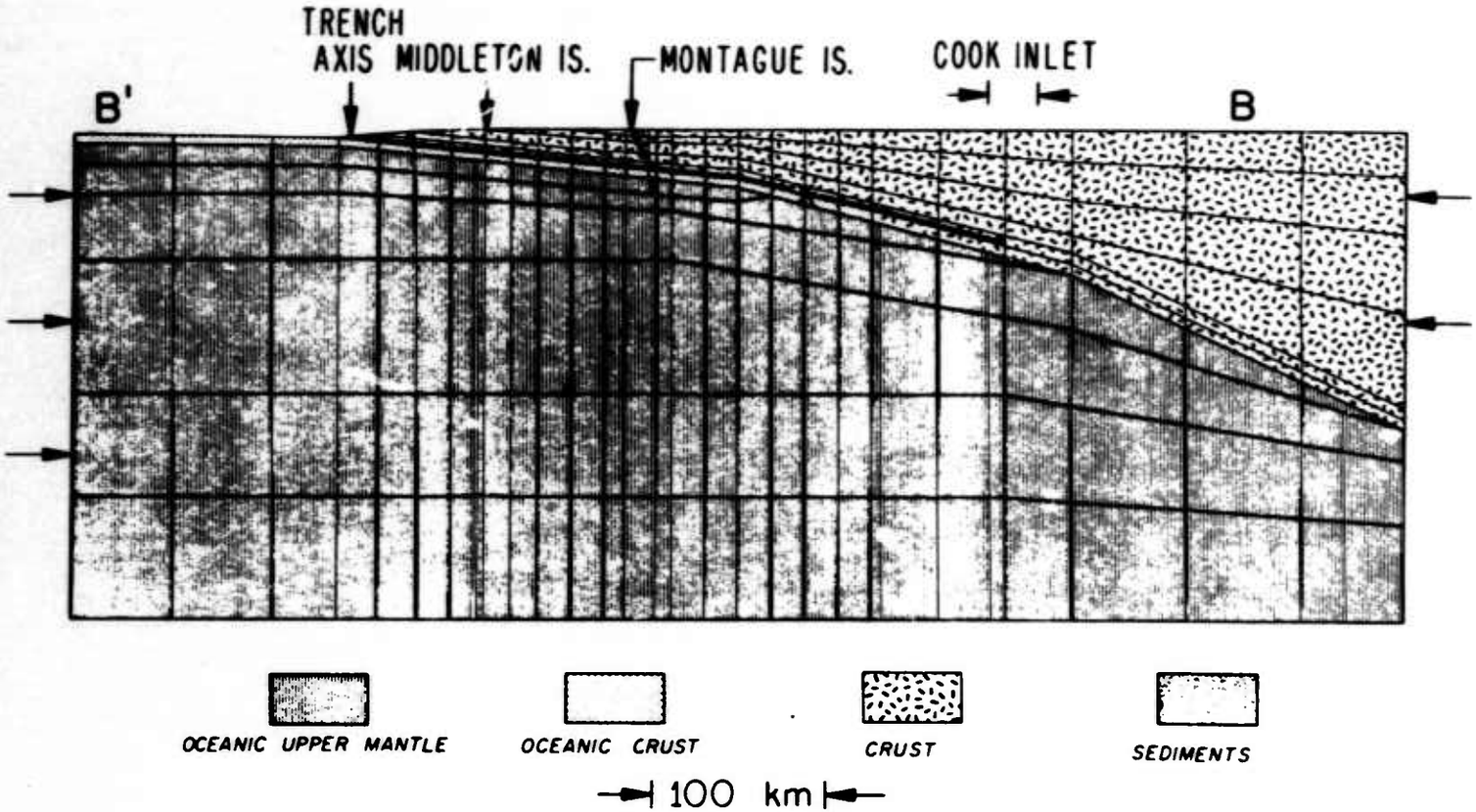

Figure 3.3. Finite element grid and structural model used. The elastic constants used are given in Table 3.1. The main fault segment and the Patton Bay fault are indicated by heavy lines. The epicenter as projected onto this profile is given by the "star". The arrows on the lateral boundaries indicate the imposed displacement boundary condition used to model the average regional prestress field expected from tectonic plate motion.

earthquake, seismic refraction studies, and the earthquake distribution of the area (Tobin and Sykes, 1966). The region is modeled by four geologic provinces, and the elastic parameters for these units have been adopted from the seismic refraction work of Shor (1962) and Hales and Asada (1966) and the microaftershock array work of Matumoto and Page (1969). The seismic velocities given in these studies are essentially those of typical crustal and upper mantle material. The velocities and elastic parameters for these units are listed in Table 3.1. Superposed upon Figure 3.3 is the finite-element grid used in modeling the fault and accompanying dislocations. The grid represents an area that is 800 km long and 300 km thick. The figure shows the Pacific oceanic plate underthrusting the continental margin beneath the eastern Aleutian arc. The majority of the material modeled in this finite element grid is that corresponding to the oceanic upper mantle. Overlying the oceanic upper mantle is a 5 km thick zone of oceanic crust which also underthrusts the continent down to a depth of about 44 km. Just under the Alaska trench we have inserted a thin layer of typical oceanic sediments. The fault model which we have assumed is at the contact between the oceanic crust and the continental crust. The fault starts under the trench with a dip of about 6° and slowly increases its dip until at a depth of 28 km the

TABLE 3.1

Unit	v_p (km/sec)	v_s (km/sec)	ρ (gram/cm^3)	μ (10^{11} dyne/cm^2)
Oceanic Upper Mantle	7.84	4.36	3.3	6.3
Oceanic Crust	6.05	3.4	3.0	3.4
Continental Crust	5.8	3.4	2.71	3.1
Trench Sediments	3.8	2.5	2.5	1.6

Table 3.1. Velocities and elastic parameters for units in the structural model of the earthquake region.

fault is dipping at 12°. The dip continues to increase so that the dip is 15° at the hypocenter and reaches a maximum of 20° below the hypocenter.

There are only two surface faults associated with this earthquake, both of which are exposed on Montague Island -- the Patton Bay fault and the Hanning Bay fault. Geologic relations (Plafker, 1967) indicate that these faults are not major geologic boundaries but rather they are subsidiary to the zone on which the primary faulting motion took place. These faults can be considered as minor imbrications of the megathrust. Both of these faults have been mapped to strike approximately parallel to the continental margin and the fault motion is reverse thrust dipping fairly steeply to the northwest. The Patton Bay fault has a large component of dip-slip motion associated with its entire length, which extends for possibly as much as 450 km to the southwest (Plafker, 1972; Malloy, 1964, 1965). Reimnitz (1966) has inferred that this fault zone extends to the northeast of Montague Island to at least Hichinbrook Island some 50 km away. The strike-slip component is measured as being less than one meter on this fault so that the motion is almost totally dip-slip. Von Huene et al. (1967) carried out seismic and echo sounder profiles in this area between Montague Island and Kodiak Island. Their results indicate a long narrow zone of faulting with the vertical attitude

of the fault plane estimated to be 60°. By the observed deformation of the sea floor, they conclude that the motion was reverse slip along this steeply dipping plane that is inclined landward. This fault is included into the structural finite-element model as a reverse fault dipping at 58° toward the continent. This fault terminates at depth where it intersects the main thrust fault at a depth of about 25 km. The second subsidiary reverse fault observed on Montague Island, the Hanning Bay fault, was not modeled in this study because of the short length (6 km) of the fault. Another high-angle imbricate reverse fault has been proposed to break the surface between the Patton Bay fault and the Aleutian trench. This fault has been inferred to explain the large vertical displacements on Middleton Island. However, no direct physical evidence confirms the existence of such a fault, and it is not included into our model. In all, a total of 26 nodes in the finite-element grid were used to represent the megathrust and the Patton Bay fault, 21 nodal elements for the megathrust and 5 nodal elements for the subsidiary fault.

3.3 Static Data.

As mentioned in the introduction to this chapter, the crustal deformation accompanying this earthquake was very extensive. Plafker (1969) has described in detail the regional vertical and horizontal displacements. (See

Plates 1 and 2 in that paper for detailed contour maps of the ground deformation and the location of the observation sites.) The vertical displacements were based on a variety of methods of measurements, some of which would be reliable only if the net vertical deformation was large, as is the case for this event. The great majority of the measurements involved measurements of the movements of the shoreline which meanders throughout the area of maximum deformation. These measurements include changes in tide gauge levels, measuring the change in the upper limit of barnacle growth, direct shoreline changes, etc.. Taken individually, these measurements cannot be given much reliability, however, when the entire mass of these observations is considered, including correlation between geodetically determined changes in bench mark levels, the data become quite informative. Plafker (1969) discusses the acquisition of this data and the associated estimate of the errors involved.

Although the vertical displacements measured after this earthquake were large, the horizontal displacements appear to be even larger (Whitten, 1964, 1965). Unfortunately, horizontal displacements do not lend themselves to the ease of facility of measurement as do the vertical displacements for this case. Parkin (1966) has described the retriangulation network that was occupied after the

earthquake. Horizontal displacements, generally in the direction of the seaward motion of the continent, of up to 20 m were observed. Pope (1972) used this data to compute the components of strain on the surface. The surveys to determine horizontal movements are too poorly controlled and too easily subject to bias to enable a detailed qualitative inversion of the strains.

In this chapter we will limit our inversion data set to vertical displacements only. The reason for this is that we consider the vertical displacement data to be much more accurate than other features of the tectonic deformation such as horizontal shortening, horizontal displacements, and changes in the local gravity field. The vertical displacement data are taken from Plafker (1965, 1969). Since with this finite-element method we are limited to plane-strain problems we will have to limit our data set to points that define a profile perpendicular to the strike of the megathrust. We chose our displacement profile to coincide with profile BB' in Plafker's papers (1965, 1969, 1972). Only one major surface fault intersects this profile, the Patton Bay fault on Montague Island. By choosing our cross section near the center of the large area of deformation, the vertical displacements are due almost totally to dip-slip motion on the fault, thus contamination of the data set due to contributions from any strike-slip motion is

minimized. By choosing the profile in this position, any effects due to the finite length of the fault are also minimized. As noted above, only slight amounts of strike-slip motion was observed along this cross section with most of it being on the subsidiary reverse faults found on Montague Island. This absence of large strike-slip motion over long lengths of the fault allows accurate plane-strain modeling of the motions involved. We also restricted the data set to those vertical displacements that could be confidently projected onto this profile. Figure 3.4 shows this cross section and the positions of the data available for projection onto this profile. The maximum distance away from the profile of a data point was about 75 km, but about 90% of the available data points were within 40 km of the profile. A total of 47 vertical displacement data points were chosen along the profile which is defined for 400 km from Middleton Island to 75 km northwest of Cook Inlet. Many more observations were available within the 40 km swath on either side of the profile, however, only those points that were not near a curve in the contours or crossed a contour were acceptable to be projected onto the profile. The projection was done parallel to the contours as defined by Plafker (1969). This projection was very close (within 10° in most instances) to a perpendicular projection onto the profile, so that the relative location

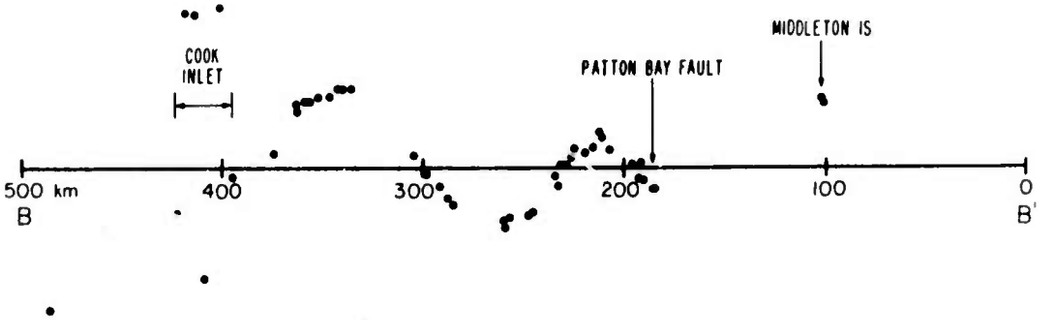

Figure 3.4. Location of the vertical displacement data points relative to the profile.

TABLE 3.2

Distance (km)	Vertical Displacement (m)	Distance (km)	Vertical Displacement (m)
101.0	3.36	259.0	-0.28
102.0	3.40	285.0	-1.20
182.0	4.56	289.0	-1.28
184.0	4.72	291.0	-1.40
184.5	7.32	298.0	-1.54
185.0	10.88	300.0	-1.62
190.0	9.16	304.0	-1.62
191.0	7.92	335.0	-1.72
192.0	7.30	339.0	-1.80
196.0	5.48	342.0	-1.75
207.0	3.22	346.0	-1.70
211.0	2.68	350.0	-1.64
212.0	2.56	351.0	-1.59
214.0	2.36	355.0	-1.52
219.0	2.32	359.0	-1.40
226.0	1.88	362.0	-0.92
229.0	1.84	373.0	-0.92
231.0	1.72	401.0	-0.30
232.0	1.68	409.0	-0.24
233.0	1.56	413.0	-0.24
235.0	1.48	418.0	-0.22
245.0	0.44	423.0	-0.24
247.0	0.50	454.0	0.00
258.0	-0.30	486.0	0.44

Table 3.2. Observed vertical displacement data along profile BB'.

of the data points on this profile can be considered accurate to within about 5 km in the most unfavorable cases. The corresponding values of the individual projected data points on the profile are given in Table 3.2. These values and their respective location along the profile will appear in several later figures in this chapter. The origin of the profile is some 100 km southeast of Middleton Island. For reference, the most southeasterly data point on Middleton Island is 101.0 km from the origin, and the profile crosses the Patton Bay fault at a distance of 185.0 km from the origin (B'). The sources of the individual data points and their associated errors are discussed elsewhere (Plafker, 1969). In general, the data are accurate to within $\pm$ 0.3 m, and this value was taken in the inversion calculations.

3.4 Calculated Dislocation Model.

The media response matrix, **A**, discussed in the previous chapter was calculated by the finite-element technique for the structural model shown in Figure 3.3. In this technique, the static displacement on the nodal segments at the free surface are linearly related to offsets imposed on the designated fault nodes. The displacement at every one of the nodal segments on the free surface due to a unit offset (1 m) on a specified fault node was calculated. This was then repeated for each of the nodes describing the

fault system. However, since the observed vertical displacement data was only near 16 of the nodal segments on the surface, the response matrix was limited to those nodes. Thus we have defined the problem of estimating the static dislocation on 26 fault nodes given the permanent static offset of 16 nodal segments located on the free surface. This is precisely the type of problem that was discussed in Chapter 2 for which we formulated the stochastic inversion scheme to solve.

In this problem, the operator **A** is a M x N matrix, where A_{ij} is the displacement, calculated at the point on the surface where the ith data point is taken due to a unit dislocation of the jth nodal segment of the fault. Here M=26 and N=16. Based on experience in calculating best model estimates by equation (2.27), it was found that much smoother, hence longer wavelength, solutions were calculated if the starting model was some "distance" in the model space away from the null model. Therefore we chose to use Stauder and Bollinger's (1966) estimate of the fault dislocation as the starting point for our inversion. This starting model turned out to be a good choice because the inversion scheme smoothly and quickly iterated convergingly to a final "best fit" model. Just to make sure that the final model that we obtained was not wholly dependent on the starting model that we chose, we then repeated the

inversion using Hastie and Savage's (1970) fault dislocation estimate as the starting model. The results were very similar to that obtained before. We therefore feel that this final model is not very dependent on the starting model.

The upper part of Figure 3.5 shows this vertical surface displacement data plotted in profile and the calculated displacement at the surface nodes of the finite element grid. The fit to the observed data is extremely good with the calculated surface displacement field fitting the observed data used in the inversion to within a RMS residual of about 3-1/2 cm, and the fit to all the points in the data set is not far from this value. For accuracy, only those data points which were very near a surface node in the finite element grid were used. Thus, out of the set of 46 data points along the profile, only 16 points could be actually used in the inversion. An increase in the number of surface nodes in the finite element grid would probably not add to the resolvability or accuracy of the slip model, since the limitations in these quantities were the lack of spatial coverage of the data, not the lack of data used. The slip model from the inversion process is shown in the lower half of Figure 3.5. The maximum slip along the fault is 33 m at a point below Montague Island. A displacement of about 30 m is maintained over a fault

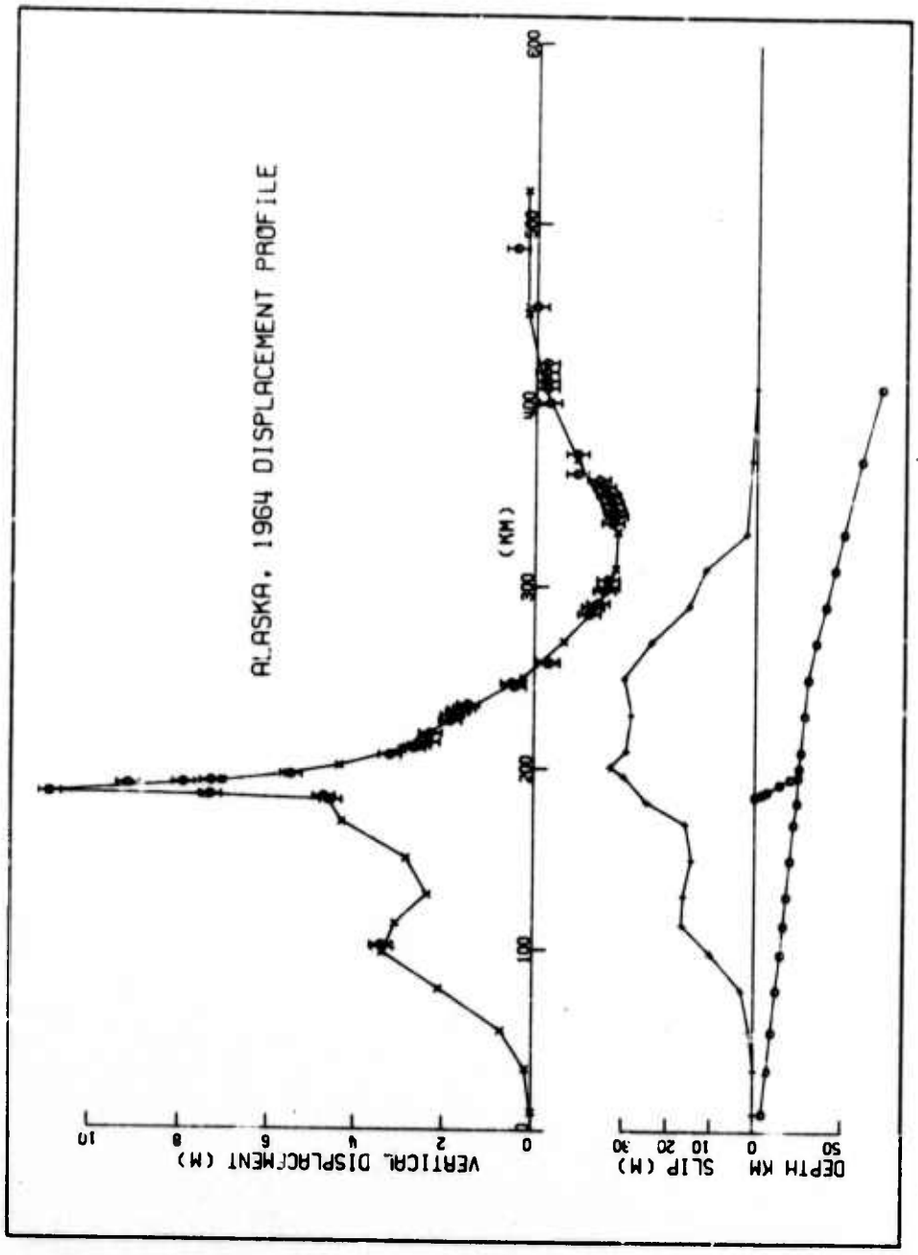

Figure 3.5. Observed and calculated vertical surface displacements and dislocations along the fault width. The dislocations plotted are offsets in a direction parallel to the fault.

width of about 60 km, then decreases almost linearly at a rate of 0.3 m/km over the next 100 km as the fault depth increases. At more shallow depths, there is a plateau in slip of about 17 m, which would correspond to the fault surface between Middleton Island and Montague Island. However, the two data points on Middleton Island are very important in this model in that their values almost completely determine the amount of slip along the top 150 km of the fault. The resolvability of this plateau will be discussed below. The slip on the secondary fault is not shown in this figure, but it averages 4 m over its entire width with the static offset on the node at the surface constrained to be equal to that measured for the scarp on the Patton Bay Fault as reported by Plafker (1967). The fault offset profile on the main fault is similar in shape to that proposed by Stauder and Bollinger (1966) who used a much simpler fault model and ignored the effects of geology.

Integrating the area under the slip versus fault width curve, we find that we have an average slip of 18.5 m over a 260 km fault width. This slip is at least 50% greater than that predicted by Stauder and Bollinger (1966), Savage and Hastie (1966), and Hastie and Savage (1970). One check to see if the average dislocation is reasonable is to calculate the average moment and compare with that

obtained from long period seismic waves. This average moment is given by

$$M_0 = \bar{u} L w \mu$$

where $\bar{u}$ is the average fault offset (18.5 m), L the length (600 km), W the width (260 km), and μ is the average rigidity of the region around the fault (3.1×10^{11} dyne/cm^2). By using the rigidity of the continental crust, the material in which most of the deformation takes place, we obtain an average moment of 0.9×10^{30} dyne-cm. Kanamori (1970) arrives at a moment of 0.75×10^{30} dyne-cm on the basis of long period (300 sec) multiple path Love and Rayleigh waves. At these long periods, the surface waves are sampling the entire fault width and thus should give a good indication of the average moment. These two values compare very favorably indicating that indeed there were very large displacements occurring along the fault surface. B. Minster (personal communication, 1973), on the basis of a systematic inversion of world-wide plate motion data, states that the Pacific plate and the Alaskan continental block are moving relative to one another at a rate of about 6 cm/year at the location of our profile.

The computed average slip on the fault leads to a recurrence time of an earthquake of this magnitude in this area of once every 300 years. However, if the central portion

of the megathrust with its average 30 m slip is used as representing the event, this gives a recurrence time of 500 years. Plafker and Rubin (1967) obtain a repeat time of about 850 years for major events on Middleton Island based on the radiometrically determined dates of a set of uplifted marine terraces found on that island. However, Sykes (1971) has expressed great uncertainty about estimations of recurrence times for major events in this region.

Although not included in the data set for the inversion, the measured horizontal displacement field was extensive. Parkin (1966) gives these horizontal movement vectors which are made with a free adjustment relative to a fixed station (Fishook station) located about 14 km north of Palmer, Alaska, an area that was then considered to be the most stable. This fixed station is 120 km northwest of the epicenter of the main shock. As in the case of the vertical displacements, only those horizontal displacement vectors near the profile line were chosen. There were 23 of these vectors in the vicinity of our section. These vectors were projected onto the profile and their component of motion in the direction of the profile taken. The resulting displacements are shown in Figure 3.6. The data points nearest the fixed station are the most accurate, being first order surveys, while the data on Montague Island are much less accurate, being based on third order

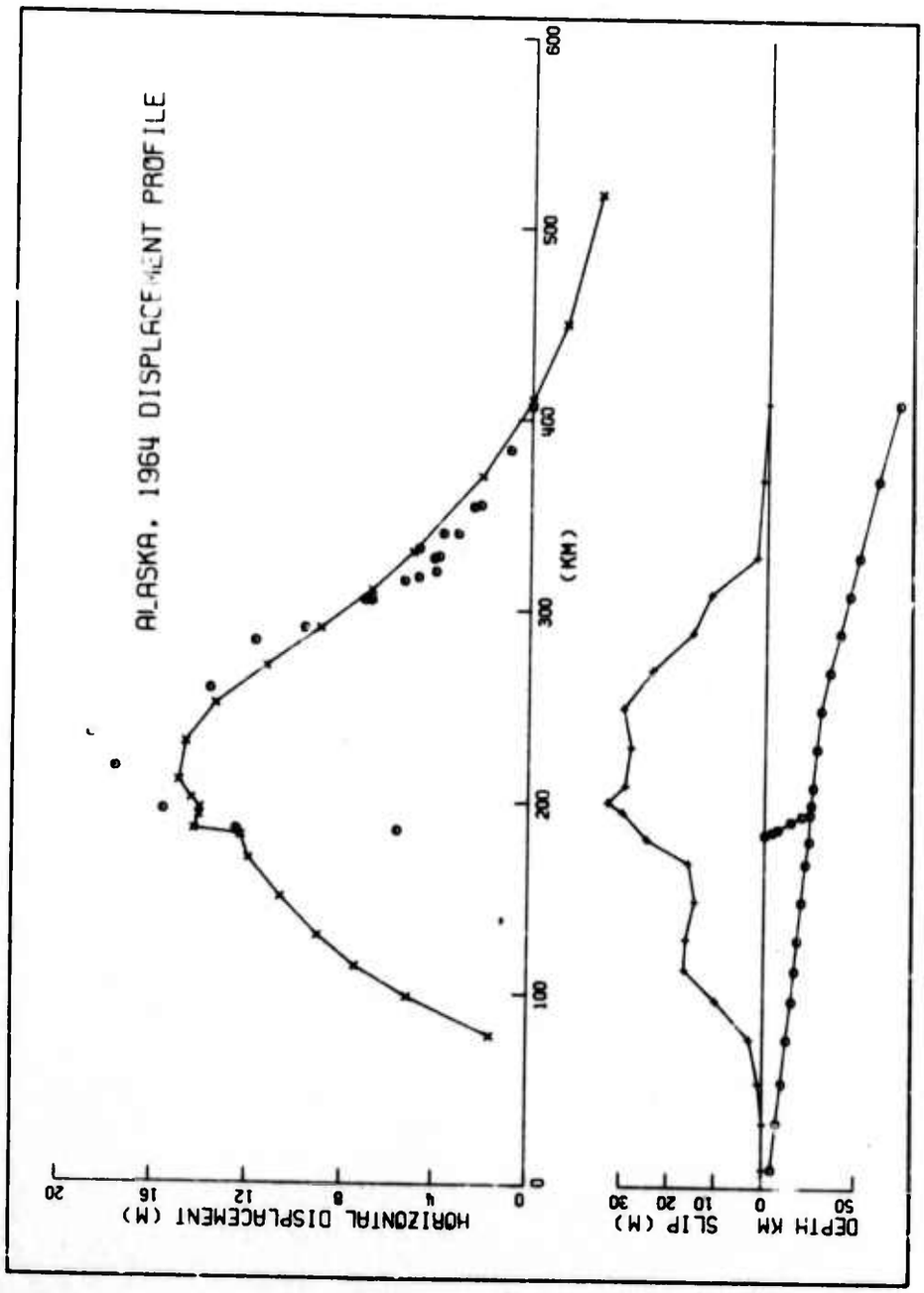

Figure 3.6. Observed and calculated relative horizontal displacements and best fit dislocation model. A positive horizontal displacement is in a direction E45°S.

observations. The direction of motion for each of these points shown is to the southeast. The horizontal displacement in this same direction is calculated from the best fit slip model discussed above and shown in the figure. These calculated points are translated relative to the displacement at the node on which the observed apparent zero isobase is projected. The resulting displacements form a smooth curve except for the irregularity at the Patton Bay Fault. This irregularity is not resolvable in the data shown here. Even though these lateral displacements were not used in the inversion scheme, because of their lack of accuracy, the fit is surprisingly good. The model predicts a movement of 4 m to the southeast at the fixed station. A stable area for displacement reference is given to be at least 120 km farther to the northwest than the chosen fixed station. The consistency of the fit to both the horizontal and vertical displacement data seems to indicate that the model geometry that was initially assumed is reasonably accurate.

Figure 3.7 shows a contour plot of the calculated displacement field in two dimensions along this chosen section. The contour values are indicated on the figure and the units are in km. In the upper half of this figure is displayed the calculated two dimensional vertical displacement (Y direction in figure). From this figure, we see that the

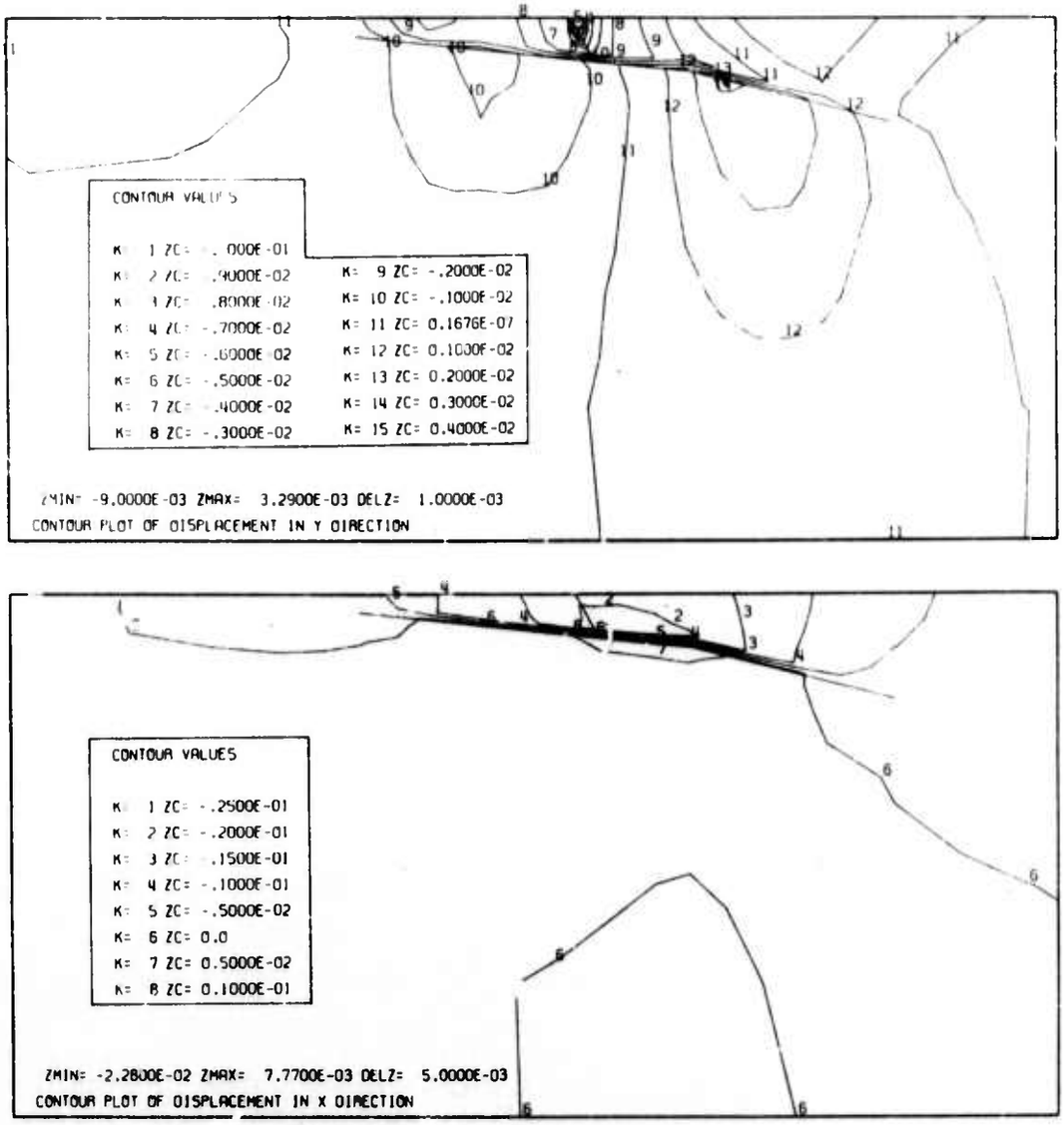

Figure 3.7. Contour plots through the cross section of relative displacement caused by the best fit dislocation solution. The contour values have units of km. The upper figure is a plot of the vertical displacements and the lower figure is a plot of the horizontal displacements.

displacement is concentrated under Montague Island and above the fault surface. The presence of the Patton Bay Fault is clearly visible on this plot. This partitioning of the displacement field is due to the effect of the nearby free surface. In the lower part of this figure, we see that the horizontal displacement (labeled the X direction in figure) is likewise concentrated immediately above the fault surface.

3.5 Resolvability of Features in the Slip Model.

Since the data used in the inversion are not perfectly accurate, there exist model perturbations which when added to our best fit slip model would still fit the observed surface displacement data to some chosen degree of confidence. If we can estimate the errors in our data, then we want to somehow relate these errors to errors in our model. Such a relation between the data space and the model space exists in the form of a variance operator (equation (2.33)). This operator is useful in this application in the following manner. If we take some perturbation, δm, to the calculated slip, then this perturbation is resolvable by the data to within a certain confidence interval if the following inequality holds,

$$\delta \mathbf{m}^* \mathbf{V}^\dagger \delta \mathbf{m} > k^2(c) .$$

$\mathbf{V}^{\dagger}$ is the generalized inverse obtained by spectral decomposition of the variance operator, and k(c) is the coefficient associated with a particular confidence interval. In this study we have chosen to examine model perturbations at the 95% confidence level, so that in this case the coefficient associated with this interval is 1.96. Using this method, we can test chosen perturbations to our calculated slip model and compute the maximum perturbation that can be resolved at the 95% confidence level by the data. We note that these tests are independent of the values of the slip model itself, and only perturbations to this model can be checked for resolvability.

The variance operator, $\mathbf{V}$, for this case is a 26 x 26 matrix. The generalized inverse of this matrix is found by using the eigenvector expansion described in equation (2.32). We found that there were 16 non-zero eigenvalues associated with this operator. For problems where the estimated errors are very small, numerical problems may be encountered in calculating the generalized inverse of this operator. These numerical problems arise from the fact that round-off errors occur in the computer calculations of the eigenvalues. For small eigenvalues, the problem of distinguishing non-zero eigenvalues from the zero eigenvalues can become serious. Fortunately, this is not the case in this problem. The non-zero eigenvalues are well

defined. We have empirically noted that the number of non-zero eigenvalues of the variance operator **V** is equal to the number of independent data points used in the inversion. The inner product of the variance operator and its generalized inverse form a projection operator. This projection operator is then checked for its idempotent properties to make sure that all scaling is correct. This test is done in the following manner:

$$(\mathbf{V}\mathbf{V}^{\dagger})(\mathbf{V}\mathbf{V}^{\dagger}) - (\mathbf{V}\mathbf{V}^{\dagger}) < \mathbf{E} \qquad (3.1)$$

where the components of **E**, ϵ_{ij}, are taken to be some small number relative to the size of the components of **V**.

The question that we would ultimately like to answer with a study of this type is, "What is the maximum pertubation that we can add to our 'best fit' slip model and still satisfy the observed data?" Since we know that the size of the maximum perturbation that is at the threshold of detection by the data depends on the distribution of the perturbation, we choose three perturbations which will elucidate the total resolvability of our slip model. We first consider how much of a slip perturbation we can add to the dislocations in the hypocentral region, so that the rapid fall-off from the 30 m plateau is not so rapid. Figure 3.8a shows this maximum slip perturbation. The

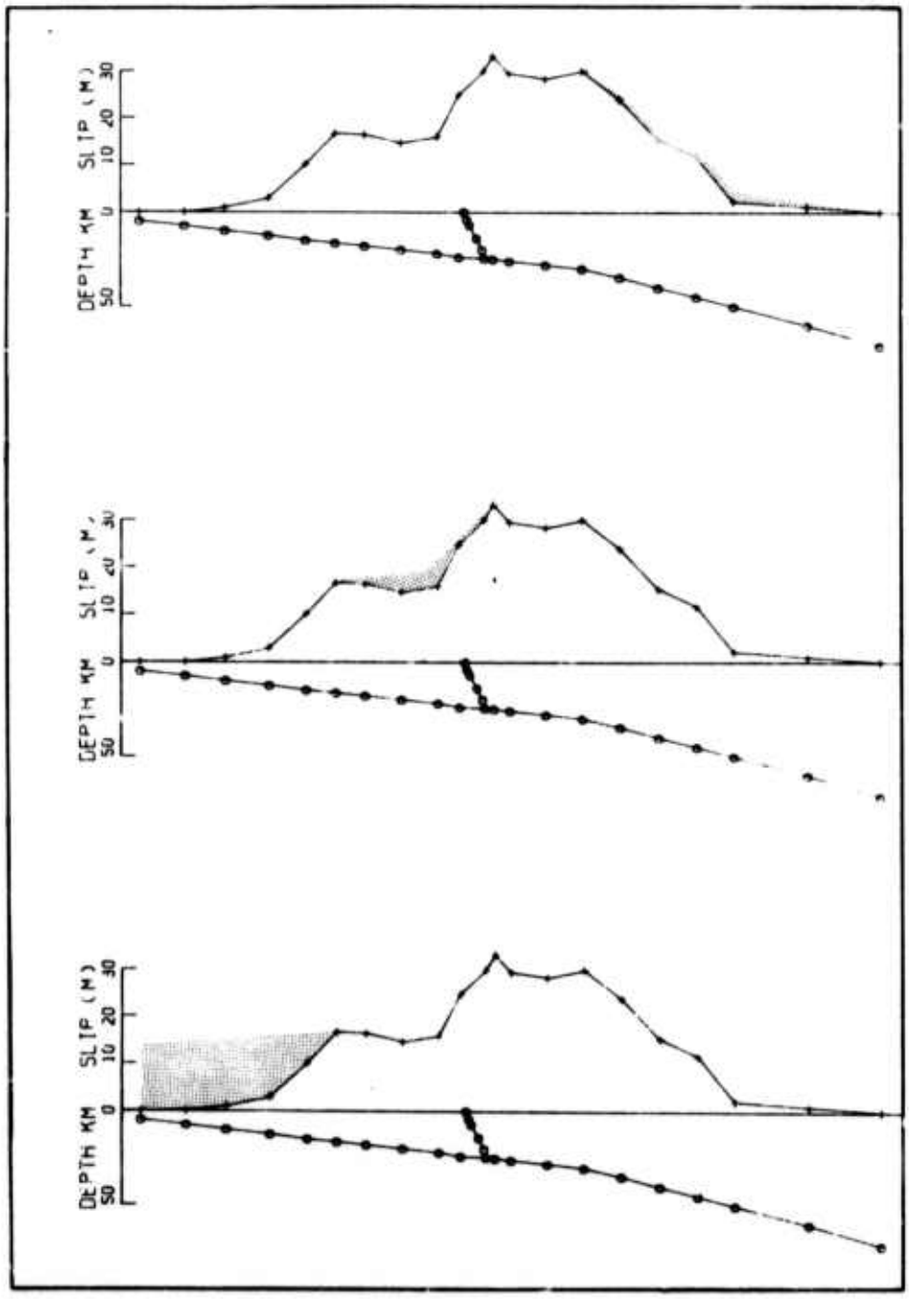

Figure 3.8. Examples of the resolvability of the best fit solution.

stippled area on this curve is the maximum slip that could be added in this region and still be undetected by the data. It is seen from the small size perturbation in this figure that the data control very closely the rate of fall-off of slip in this area of the fault. This is due mainly to the fact that there is a dense network of data points just above these particular nodes. Next, we try to determine if the data demand the existence of the 17 m plateau in the shallow part of the fault. Figure 3.8b shows the amount of slip that could be added in this region. We see that the slip gradient in this region could be smaller than that presented in our best-fit slip model, although there still appears to be a requirement for a sharp decay in slip up the fault from the 30 m plateau. The slight minimum in slip that appears in this region of the model is not resolvable by the data. In Figure 3.8c we see that there is almost no resolution along the upper part of the fault. This is due to the paucity of data on the surface above this region. In order to explain the behavior of the fault slip in this region we have to appeal to arguments based on other geophysical data than the statical displacements. For instance, it can be shown that large fault offsets in the area of the trench would result in a significant amount of strain energy stored by the fault in that region.

3.6 Averaging Operators.

In Chapter 2 we say that our "best fit" estimate of the slip model is in reality some filtered average of the true slip model. This filtering operator is commonly known as the averaging operator. Before discussing features of our final model it is to our advantage to know the extent of the averaging that is taking place in our model. The kernels of the averaging operator are taken to be individual rows of the operator matrix, **R**, as defined in equation (2.29), with a single kernel being defined for each fault element comprising the total fault system. We note here that if the problem is linear, as it is in this case, that these kernels do not depend on the final estimate of the "best fit" model.

If a particular slip model value were perfectly well-known by the inversion then the averaging component centered on that fault element would be unity and all the other components of this kernel would be zero. However, in the general case where we have less than infinite data and the data that we do have are somewhat corrupted by noise, the center averaging values are not unity and the other components (off-diagonal components of the matrix **R**) are non-zero. The ability to resolve the details of the actual dislocation function depends on two features of this operator. One is the size of the kernels. This depends

in a general way on the availability of data to be included into the inversion that are sensitive to a dislocation over the part of the fault model that we are testing. As the value of a particular diagonal component of **R** becomes substantially less than unity, our ability to even estimate the slip value for the corresponding model component decreases. The other factor is the averaging width of the kernels. This averaging width is expressed by the off-diagonal elements of **R**. If these off-diagonal components, corresponding to the fault elements "near" the particular fault element we are examining are substantially non-zero, then the estimated "best fit" value of slip that we obtain from the inversion is really some linearly averaged value of the actual slip values in the vicinity of this fault element. These ideas are probably best expressed by examining an example of their use.

Figures 3.9 and 3.10 show examples of the averaging kernels for the Alaska earthquake model. The coefficients of the rows of the averaging operator are shown diagrammatically at the position of the respective fault node corresponding to the components of this row. The height of the bar plotted on each node signifies the absolute value of the averaging coefficient for that node. For absolute reference, in Figure 3.10c, the height of the outstanding bar is 0.997. In Figure 3.9, we have plotted

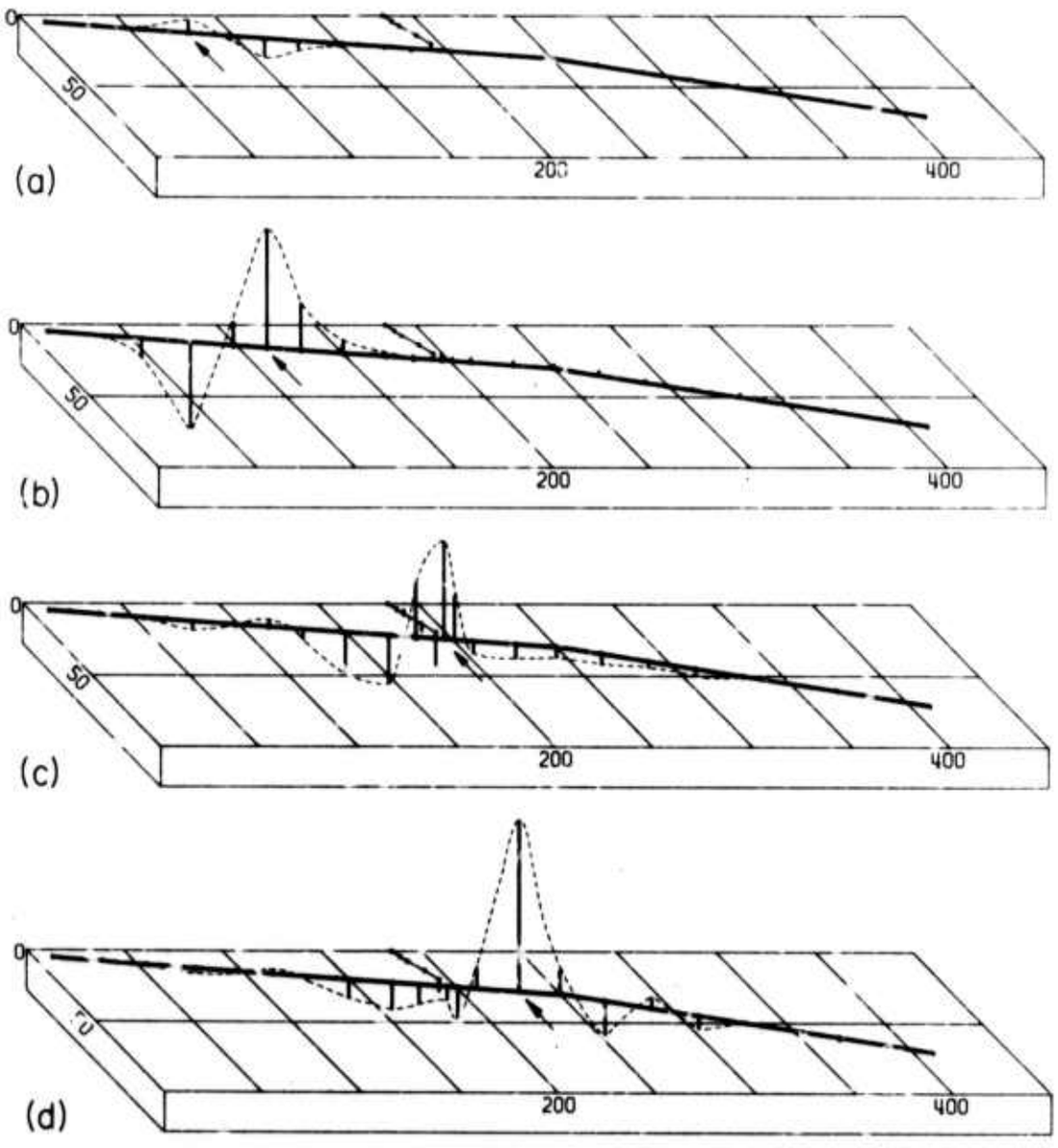

Figure 3.9. Resolving kernels for selected nodal segments along the megathrust. View is a perspective of the megathrust from the southeast (left) to the northwest (right). Depths and profile distances are in km.

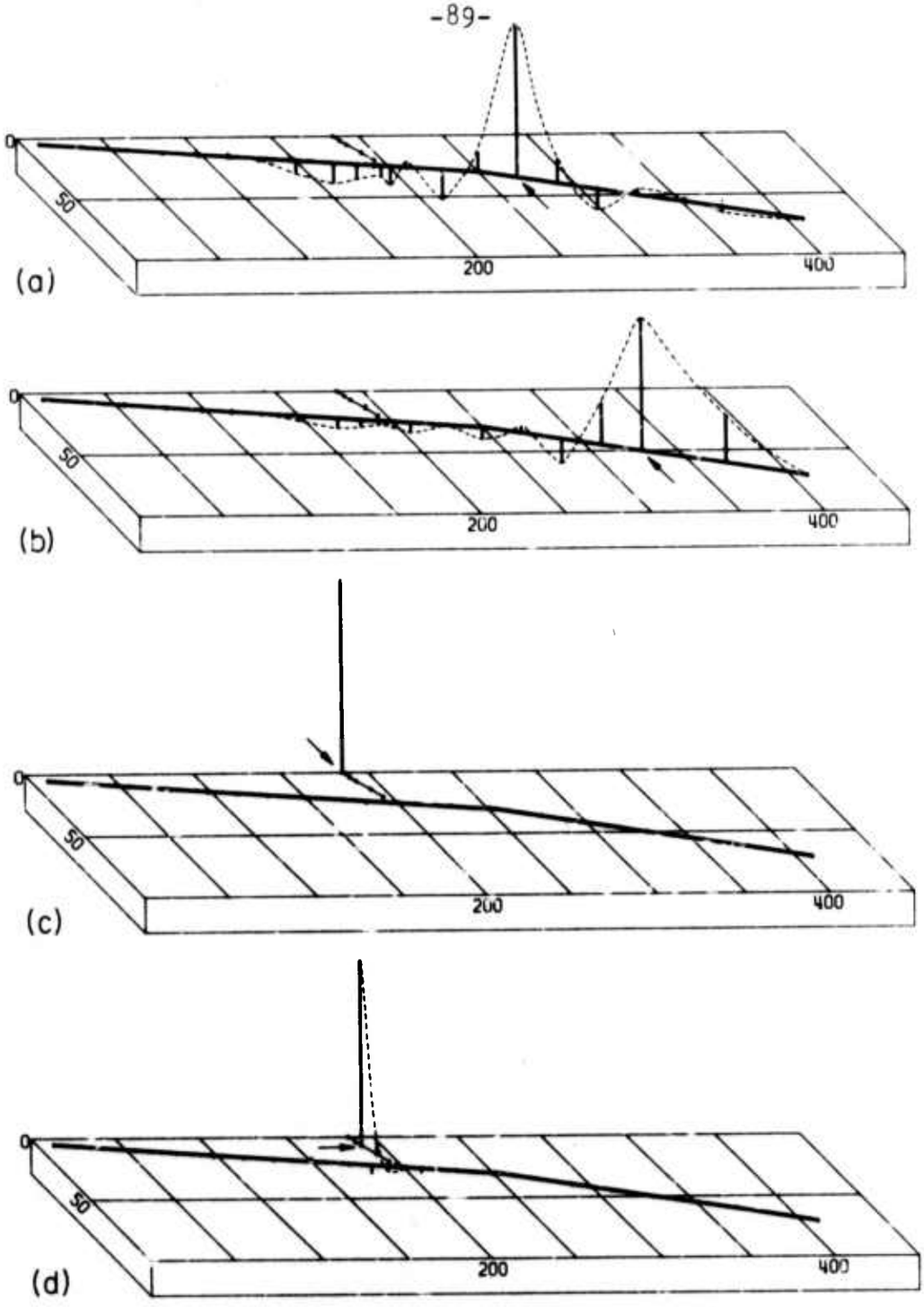

Figure 3.10. Resolving kernels for selected nodal segments along the megathrust (a,b) and subsidiary fault (c,d). View is a perspective of the megathrust from the southeast (left) to the northwest (right). Depths and profile distances are in km.

the averaging for representative nodes along the megathrust presented here in a perspective view. The arrow in the figure indicates on which node the averaging is centered. In Figure 3.9a we see that for the upper part of the megathrust, the averaging values are very small, again showing our lack of resolvability in this area of the fault. In Figure 3.9b the kernel values are larger in amplitude indicating our ability to estimate the slip in this portion; however, we see that there are large side lobes. The negative averaging coefficient, indicated by the bar extending downward, means that a positive dislocation on the centered fault node could be traded off with a negative dislocation on this node, and the data would not be able to tell the difference. In Figure 3.9c we see that the averaging over the adjacent nodes to either side of the central node is fairly severe, and that there is a slight amount of coupling to the subsidiary fault. In the bottom figure, we see that the amplitudes start to become more peaked, indicating better resolvability. We also note that the slip in this area is completely uncoupled from the slip on the subsidiary faulting. This shows how the effect of the subsidiary fault is very localized with respect to the megathrust.

The examples are continued in Figure 3.10. Sections a and b of this figure continue to show that on the lower part of the megathrust we are able to determine fairly well

the "best fit" estimate of the slip, but this slip is generally averaged over the one or two adjacent nodal segments. Figure 3.10c shows the averaging kernel for the top most nodal segment of the representation of the Patton Bay fault. Here, the displacement is almost exactly determined. The height of the bar is almost unity, 0.997, and there is practically no spatial averaging. We would expect this result, considering that this fault segment breaks the surface and the amount of dislocation on this nodal segment is constrained by the scarp size on Montague Island. Likewise in Figure 3.10d, the dislocation at some depth on the subsidiary fault is well determined, and there is practically no trade-off in dislocation here to a dislocation on the megathrust.

The information contained in the averaging operator can be summarized by defining a resolvability ratio for each kernel. This ratio is defined as the ratio of the value of the diagonal coefficient of **R** to the averaging half-width. This averaging half-width, though somewhat ambiguous in some instances because of asymmetries, can usually be estimated,however. The averaging half-width is measured from the central fault node to the point where the averaging first crosses zero. This ratio is convenient and meaningful in the sense that it takes into account both the variables involved in estimating resolvability: the height

of the kernel and the averaging distance. For well resolvable features of our model we would expect large ratios; for less well resolvable features, smaller ratios. The results for this particular fault model are shown in Figure 3.11.

In this figure, we see that for the upper 75 km of the megathrust, there is a total lack of resolvability, controlled by the lack of data which are sensitive to a dislocation in that area. The resolvability is slightly peaked for the area of the megathrust immediately under Middleton Island, but again there is no resolvability in the area between the islands. The resolvability decreases rather evenly for the lower end of the megathrust. This is thought to be due to the fact that the dislocations are occurring at distances farther and farther away from the data, thus dislocation averaging starts to become a problem and the resolvability is reduced.

3.7 Stress and Strain Energy Density Change.

In terms of understanding the focal processes of earthquakes, an important parameter is the stress drop. In previous studies of earthquakes, the stress drops were obtained through empirical formulas or exact derivations for special purpose geometry of the crack (for example, Starr, 1928; Knopoff, 1958; Aki, 1966). The stress drop over some fault dislocation area is usually given by the following

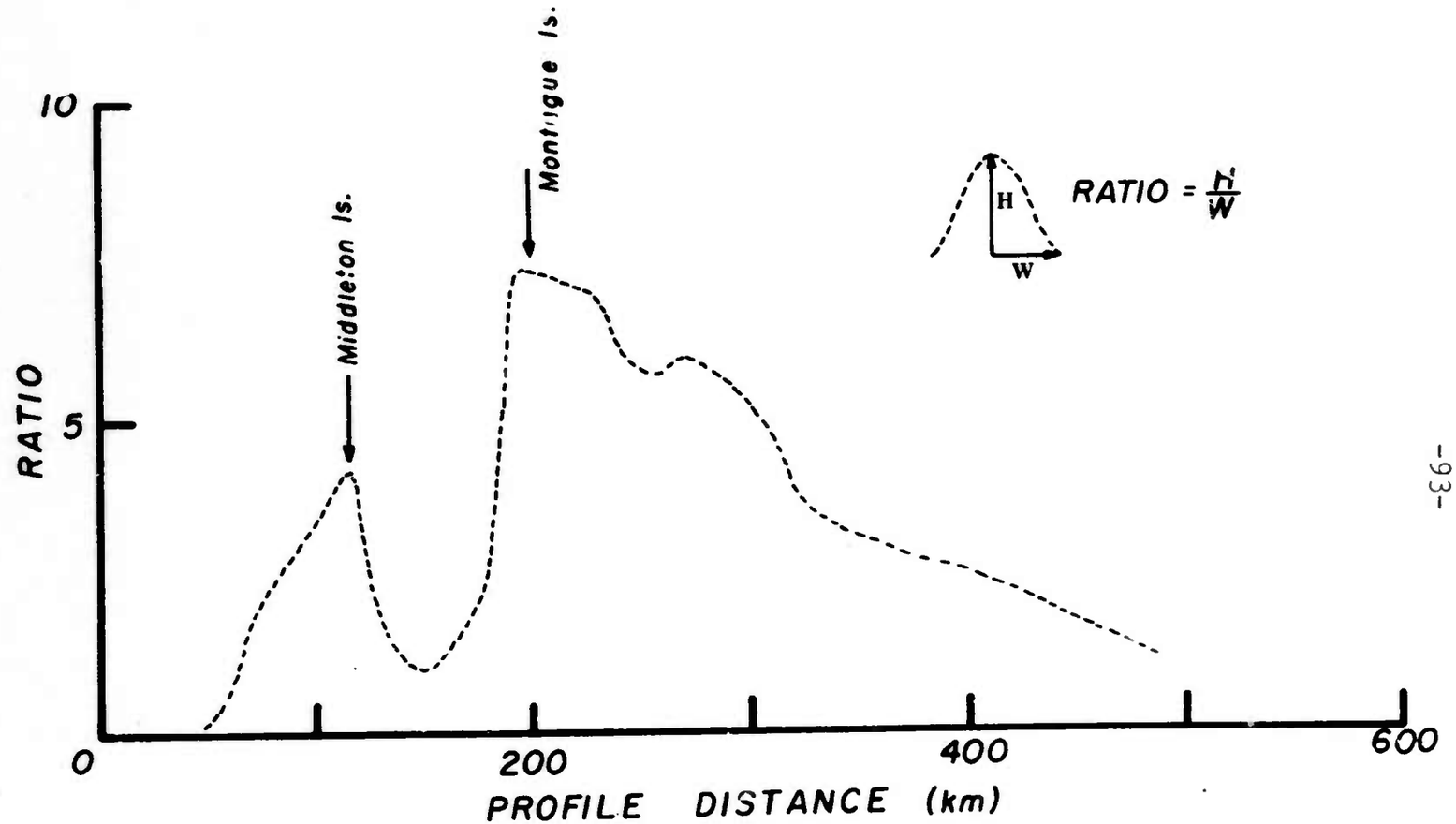

Figure 3.11. Resolvability ratios for the nodal segments along the megathrust plotted as a function of their projected distance along the profile BB'. Large values of this ratio indicate good resolvability and vice versa.

type relation,

$$\Delta\sigma = \frac{\eta U_m \mu}{W} \qquad (3.2)$$

where μ is the rigidity, U_m is the maximum displacement, W is some measure of the size of the fault, and η is some constant dependent upon the geometry and nature of the faulting. Use of this formula results in stress drop values that are averaged over the entire fault plane. For instance, Brune and Allen (1967) estimate the stress drop from the average offset given by Savage and Hastie's (1966) dislocation of the 1964 Alaska earthquake to be 27 bars. In this calculation, η is taken to be 1.33, W=200 km, U_m= 13.3 m, and $\mu=3.0 \times 10^{11}$ dyne/cm^2. If we were to use their formulation with our average dislocation, we would obtain a stress drop of 30 bars. Chinnery (1969) and Sato (1972) point out that in order to evaluate η the assumption of an infinite length fault is usually made. These two authors have derived the expression for the stress drop for a finite rectangular fault, and they show that the stress drops obtained for these faults are smaller than what one would obtain for infinite length faults. For the Alaska earthquake, Sato (1972) estimates η to be 0.97 when a constant displacement over the fault surface in an idealized medium is considered. His resulting estimate of the

stress drop using this parameter and our average dislocation would be about 22 bars. This last value is still an estimate of the stress drop averaged over the entire fault surface. However, it is obvious that if the dislocation is varying over the fault plane, and the geometry of the plane changes with distance, the stress change will not be a constant over the entire fault surface. Jungels (1973) has shown that for several earthquakes the stress drop can vary along the fault by as much as an order of magnitude.

To estimate the stress drop along the width of the fault we can apply equation (3.2) to each of the nodal segments which define the fault plane, but there is always uncertainty in the estimate of the parameter η. Jungels (1973) has shown a more direct method of calculating the fault stress drop distribution with the finite element method. This is accomplished by first imposing a composite prestress field on the structural model. This is done by applying a dislocation to the edges of the structural model. From this initial state, we can compute the equilibrium final state that would be caused by the introduction of our best fit dislocation model. Then, at every point of the structure, the difference between the initial and final stress fields defines the stress change. If $\Delta\sigma$ is positive, then the particular model caused a stress drop. If $\Delta\sigma$ is negative, then we have a stress increase.

it is clear that for a "dislocation" model the magnitude of the stress change is controlled only by the magnitude of the fault offset and the elastic constants of the structural model. Thus the prestress only has importance in terms of the strain energy change where the sign of the stress drop matters. The shear stress change approximately parallel to the megathrust is calculated by this method and is contoured throughout the cross section studied. (Figure 3.12). The values contoured are exact away from the fault plane, but for the nodes defining the plane itself, the actual stress drop is approximately twice the value shown. This error arises from the fact that a linear behavior of displacement is assumed inside each element in the finite-element grid. This error results in an underestimate of the stress change on the fault surface (Jungels, 1973). Assuming that the error is exactly a factor of 2 in this problem, we see that for our best fit model the stress change along the fault itself varies from a stress increase of 86 bars to a stress drop of 215 bars. The stress change over the entire width of the fault averages a stress drop of approximately 40 bars. This indicates how misleading a value of the average stress drop could be.

The details of the stress change are very interesting. We see that both ends of the fault underwent a net increase in shear stress. For the shallow portion of the megathrust

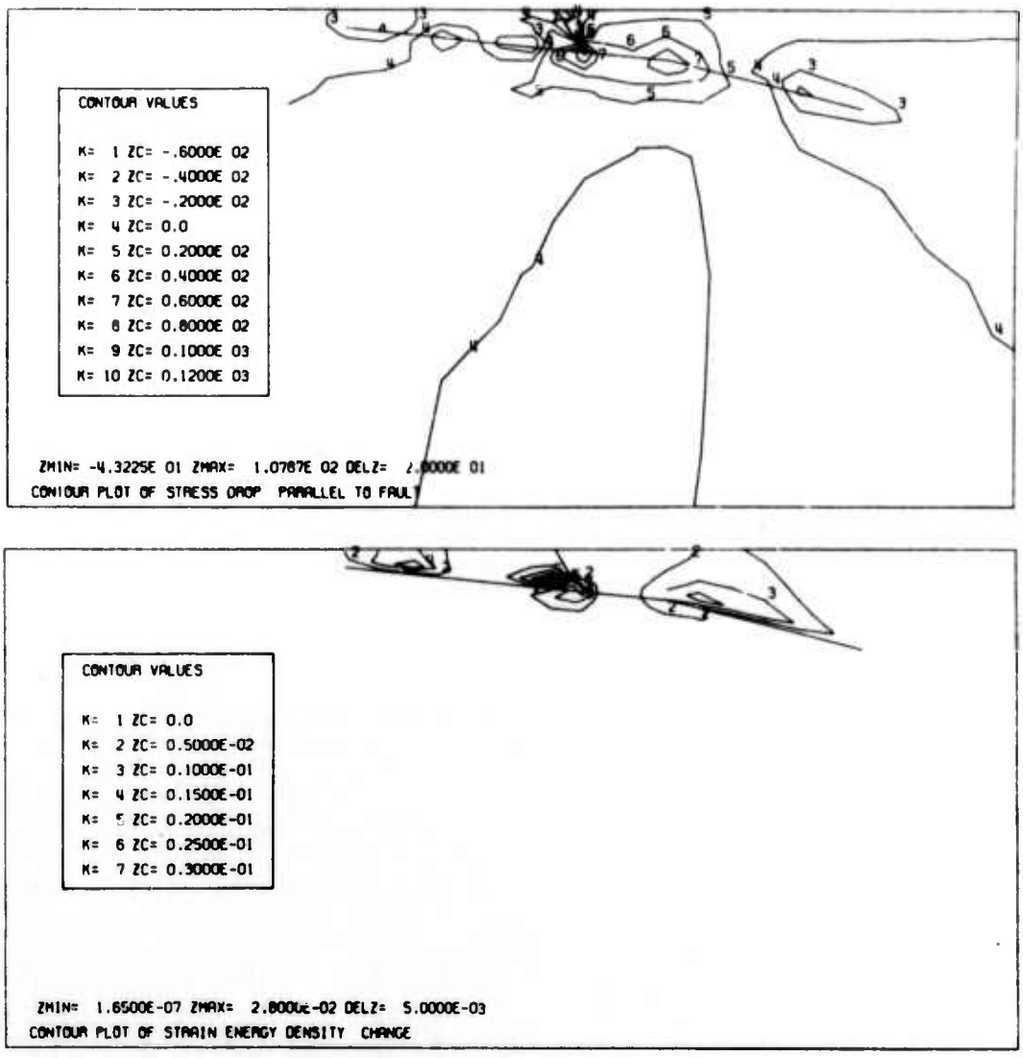

Figure 3.12. Stress change and strain energy released around the fault surface for an average prestress level equal to the average stress drop. Positive contour values of stress change represent stress drops. Units are bars and 10^{21} ergs per km^3.

this is an argument in favor of our best fit solution with its small offset in this region. It follows that if we increased the offset on the shallow end of the fault, even though we could not resolve this increase with the surface data, the stress change would increase in proportion and this in turn would make that region a prime candidate for aftershock activity. The fact that significant aftershocks were not observed here (Algermissen et al., 1972) argues for our best fit solution. On the other hand, if the offset at the shallow end of the megathrust were the maximum amount indicated on Figure 3.8, in all likelihood the displacements would rupture the free surface. If this was the case, the stored stress would be relieved and thus there would be very little or no aftershock activity. A search of the literature concerning this earthquake revealed that there seems to have been no post-earthquake reconnaissance of the ocean floor in the vicinity of Middleton Island and further toward the Aleutian trench, so that the possibility of this occurring cannot be ruled out. A hydrographic and ocean-bottom-scanning sonar survey of the area to the southwest of Montague Island revealed fresh scarps on older en echelon faults sub-parallel to the extension of the Patton Bay fault (Malloy and Merrill, 1969.) These authors attribute these scarps to the Patton Bay fault system. It is conceivable that much of the strain

from the large dislocations on the very shallow end of the megathrust could be relieved in this fashion. That is, large displacements on the fault surface are absorbed through a system of high angle bifurcations of the main thrust sheet. We will see in the next chapter that this is precisely what occurred during the 1971 San Fernando, California earthquake. Unfortunately, for the Alaska earthquake, the data are not adequate to prove or disprove that this condition existed, and further speculation along these lines seems fruitless.

Another area of slight stress increase on this figure is found in that region where the offset function in the best fit model goes through a local minimum between the 30 m slip plateau and the 17 m slip plateau. We have seen from the above discussion, however, that this minimum is not resolvable, so therefore the existence of the stress increase in this region is not resolvable by the data. Most of the stress drop along the fault surface occurs where the fault dislocation is the greatest. The maximum stress drop, 215 bars, is found along the megathrust just below the intersection of the Patton Bay Fault.

A plot of the strain energy density change in the media as seen in the lower half of Figure 3.12 illustrates that most of the energy available for seismic radiation would come from the central area of the megathrust in the

same region where the maximum stress drop occurs. The contours in the figure are in units of 10^{21}ergs/km^3. A direct comparison can be made between this strain energy density plot and the multiple rupture characteristics that Wyss and Brune (1967) found for this event. These authors interpret the P-wave radiation as caused by a multiple event source mechanism whereby the rupture initiating at the hypocenter travels up the fault plane triggering discrete seismic events larger than the initial event. The largest of these discrete events has been located on the megathrust 20 km southeast of Montague Island. The pulse from this region was delayed from the initial pulse by a time corresponding to a rupture velocity of 3.5 km/sec and had an amplitude significantly larger (up to 30 times larger) than that radiated by the initial shock. This agrees qualitatively with our estimate of a large strain energy density change of up to 0.28 x 10^{20}ergs/km^3 concentrated below Montague Island, while in the hypocentral region, the energy density change is computed to be only 0.02 x 10^{20}ergs/km^3.

3.8 Accuracy of the Plane-Strain Approximation.

We would like to somehow approximate the errors that occur by making the plane-strain approximation that we have taken in this example. One way of getting an estimate of this error is to approximate the fault model by a series of

three-dimensional Volterra planes and to use the static dislocation theory (Smylie and Mansinha, 1971; or equation (2.2)) for a three-dimensional fault in a homogenous half-space. Although this model will not have the influences of the lateral heterogenities included, it will serve to estimate how good or bad the approximation is that we have made. A Volterra approximation to the finite-element structural model was made. This model consisted of 22 individual fault elements, 18 to describe the megathrust and 4 to describe the subsidiary faulting. The Volterra fault elements are planar surfaces centered on the position of the finite-element fault nodal segments and extending halfway to the adjacent fault nodal segments. Only those fault nodal segments were modeled on which there was a calculated non-zero displacement. Several of the nodal segments, at the shallow end of the megathrust and at the very deep end of the megathrust, had "best fit" dislocation estimates of zero. These segments were not modeled with the Volterra approximations. The dislocation which is constant over the planar surfaces was taken to be equal to that of the finite-element fault nodal segment at the center. The parameters for this model approximation are given in Table 3.3.

We first calculated the vertical displacement for a profile due to this fault model with the length of each

TABLE 3.3

Fault Segment	Dip (deg)	d (km)	W (km)	$\langle \Delta u \rangle$ (m)
1	6.0	8.5	22.8	0.99
2	6.0	11.0	21.4	2.93
3	6.0	13.0	18.0	10.17
4	6.0	15.0	16.2	16.72
5	6.0	17.0	18.2	16.39
6	6.0	19.0	20.1	14.66
7	6.0	21.0	16.0	16.05
8	6.0	22.5	13.0	24.91
9	6.0	24.0	9.7	29.98
10	6.0	25.0	7.1	33.22
11	6.0	26.0	14.2	29.42
12	6.0	27.5	20.0	28.28
13	8.0	29.5	20.0	29.99
14	11.5	32.5	20.4	23.91
15	14.0	36.5	20.4	15.35
16	15.0	41.5	20.8	11.70
17	15.0	47.0	31.2	2.17
18	15.0	55.5	41.6	1.03
19	58.0	0.0	2.4	4.05
20	58.0	2.0	4.0	3.31
21	58.0	5.5	5.8	7.18
22	58.0	10.5	8.0	2.83

Table 3.3. Source parameters for the 3-dimensional homogenous approximation to the finite-element model of the Alaska earthquake. d is the depth to the top of the planar fault surface; W is the width of the fault surface measured along the dip; and $\langle \Delta u \rangle$ is the fault dislocation.

planar surface taken to be 10,000 km, or effectively infinity, to thus approximate the plane-strain criterior. The profile was taken to be equi-distance from the ends of the fault elements and perpendicular to the strike of the system. The vertical displacements in a profile were then calculated from this fault system but now the lengths of the individual fault elements were set to 600 km, the approximate lower limit for the fault length estimated to be appropriate for this event. The profile was taken, not across the center of the fault system, but at a position 80 km from the center and still perpendicular to the strike of the fault system. This profile is 220 km from one end of the fault and 380 km from the other end. This is approxmately the maximum distance profile BB' in Figure 3.2 can be considered from the center of the fault system. The estimated errors arising from the plane-strain approximation was taken to be the difference between the computed displacements for these two profiles. This difference is a function of the distance away from the origin of the fault system. The origin of the fault system is taken to be the point at which the shallow end of the megathrust projects to the surface. The differences are presented in Figure 3.13a. It is seen from this figure that the maximum displacement error expected from the plane-strain approximation would be about 0.35 m for this particular model. The

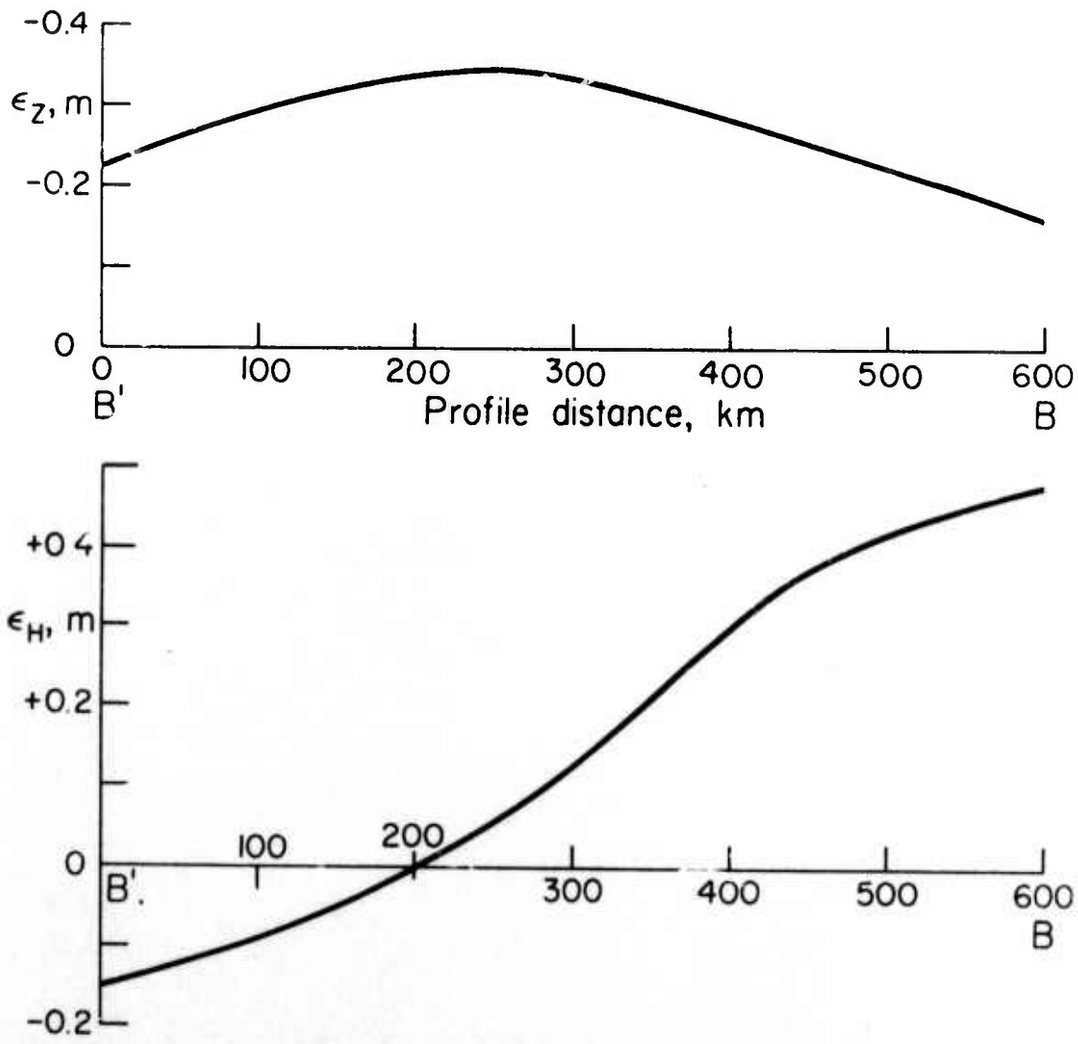

Figure 3.13. Estimates of the errors to the calculated vertical displacements (top) and horizontal displacements (bottom) due to the plane-strain assumption as a function of distance along profile BB'.

differences between these two profiles are relatively constant at about 0.25 m, and the sign of the error is such that the deformation at the surface is being underestimated. This implies that the free surface displacements for a fault dislocation model with a finite size length are slightly larger than those from a model in which each fault component has infinite length. Thus, we can say that the displacements calculated for the finite-element model are an upper bound to that necessary to fit the data. Considering the finiteness of the length of the actual fault, we would need only slightly less displacement on the megathrust.

Now the horizontal displacements are put to the same test. Horizontal displacements in the direction perpendicular to the strike of the fault system from the Volterra dislocation model were calculated for both a profile due to an infinite length fault and for a profile 80 km away from the center of a fault system that has fault element lengths of 600 km. Figure 3.13b shows the differences between the former and the latter profiles. It is seen here that as the profile distance becomes greater than half the fault length, the errors due to the plane-strain approximation start to become more significant. It is seen here that for the farthest distance along the profile, the expected error in the calculated horizontal displacements

is about 0.5 m. The sense of this error is that the estimated horizontal displacements made under the plane-strain criterior are too large. Thus in Figure 3.6 where we estimated that the reference station for the measured horizontal displacements (Fishook station) actually moved 4 m to the southeast, we have to revise this estimate to be about 3.5 m. The area of horizontal stability, that is, the area where no horizontal movement was expected, is still some 75-100 km to the northwest of the reference station.

We will now briefly examine the implications of the estimated error due to the plane-strain approximation. Since only the vertical displacements were actually used in the inversion procedure, only the errors associated with these measurements will affect the resolution of our model. Since the estimated errors due to the plane-strain assumption affecting the data points used in the inversion were about equal to the estimated observational error of the data themselves, we can estimate that at most, the total variance of the data should be multiplied by a factor of 4. As we can see from equation (2.33), if we want to recognize a given perturbation to our model at the same confidence limit as before (95%), then the size of the perturbation will have to be doubled. This means that in Figure 3.8 the amplitude of the stippled area will be doubled if we keep the shape of the perturbation as before. This implies

that the steepness of the rate of dislocation fall-off with distance from the maximum plateau going toward the hypocenter is not quite as resolvable as before. For the other two perturbations considered, the conclusions arrived at before are unchanged.

3.9 Conclusions.

A dislocation model has been presented for the 1964 Alaska earthquake. The surface displacements from this model are calculated with the finite-element numerical modeling technique in which the effects of both the known geologic heterogeneities of the region and the non-linearity of the assumed fault plane are taken into account. The dislocation model, which was obtained using a stochastic inversion scheme, fits with high precision both the observed vertical and horizontal displacements. The calculated static offset along the fault plane was found to be variable and to have a maximum amplitude much greater than previously imagined, although the average moment agrees with that observed from long period surface waves. The two-dimensional displacement field was found to be strongly partitioned above and below the fault surface, with most of the displacement occurring above the fault. The calculated displacement at the shallow end of the fault model was found to be almost non-resolvable due to the lack of surface displacement data, while the displacement near the

hypocenter was well constrained by the data. Along with the displacement calculated along the fault surface, both the stress drop and the strain energy density varied widely. The maximum stress drop found was 218 bars, while at both ends of the fault the stress field increased as a result of the static dislocations. The region of maximum stress drop and maximum strain energy density change calculated from this static study was found to correspond to the region of maximum compressional wave radiation. The errors caused by the plane strain approximation for this event were analyzed and found not to affect any of the above conclusions.